Korean J. Chem. Eng., **28**(9), 1797-1813 (2011)
DOI: 10.1007/s11814-011-0213-3

INVITED REVIEW PAPER

Zinc oxide nanostructures and their applications

Yoon-Bong Hahn†

Department of BIN Fusion Technology, School of Semiconductor and Chemical Engineering,
and BK 21 Centre for Future Energy Materials and Devices, Chonbuk National University, Jeonju 561-756, Korea
(*Received 15 August 2011 • accepted 20 August 2011*)

Abstract–Zinc oxide (ZnO) has been known as the next most important material for the fabrication of efficient nanodevices and nanosystems because of its versatile properties such as semiconducting, piezoelectric, and pyroelectric multiple properties. In this review, the state-of-the-art technologies related to the synthesis and characterization, the selective growth of ZnO nanostructures, and their applications for nanodevices are discussed. A special concern is focused on the controlled selective growth of ZnO nanostructures on wanted areas of substrates, which is crucial factor for devices applications. The device applications of ZnO nanostructures include field effect transistors (FETs), field-emission devices, piezoelectric nanogenerators, biosensors, p-n heterjunction diodes such as light-emitting diodes and photovoltaic cells, and so on.

Key words: Zinc Oxide, Nanostructures, Growth Methods, Device Applications

INTRODUCTION

Zinc oxide (ZnO) is a fascinating material with versatile properties which are suitable for high-technology such as light emitting diodes, photodetectors, photodiodes, optical modulator waveguides, chemical and bio sensors, varistors, energy harvesting devices including solar cells and nanogenerators, electromagnetic coupled sensors, actuators, and so on owing to its wide band gap, chemical and thermal stability, electronic, optoelectronic and piezoelectric properties [1-10]. ZnO also has a great diversity in structural morphology, probably the richest family of nanostructures among all materials both in structural and properties viewpoints [11-14]. Therefore, it has received broad attention from scientists, which has led to the publication of thousands of research papers and hundreds of patents.

ZnO is also an attractive material for short-wavelength optoelectronic applications owing to its wide band gap of 3.37 eV, large bond strength, and large exciton binding energy (60 meV). Therefore, it is suitable for efficient excitonic emission at room-temperature and solid-state blue to UV optoelectronics, including laser developments. The optical transparency to visible light of ZnO also provides it an opportunity to replace conventional transparent conductive indium-tin oxide (ITO) and to develop transparent electronics, transparent energy harvesting devices, and integrated sensors.

In addition, ZnO has a wide morphological diversity in nanostructures such as nanowires [15,16], nanorods [17], nanotubes [18], nanobelts [19], but also other complex morphologies [20]. Such nanostructures are rather easily grown at relatively low temperatures and various growth methods have been reported for the synthesis of ZnO nanostructures, including chemical and physical methods such as thermal evaporation [21], chemical vapor deposition (CVD) and cyclic feeding CVD [22], sol-gel deposition [23], electrochemical deposition [24], hydrothermal and solvothermal growth [25], surfactant and capping agents-assisted growth [26]. Thanks to the aforementioned fields and applications and growth techniques, ZnO could be one of most important materials for future research and applications.

In this review, the state-of-the-art technologies related to the synthesis, characterization, and devices applications of ZnO nanostructures will be discussed. Especially, applications to optoelectronics, energy harvesting, and chemical and bio sensors are to be focused.

CRYSTALLINE STRUCTURE AND PHYSICAL PROPERTIES OF ZnO

The crystalline ZnO has a wurtzite structure that has a hexagonal unit cell with two lattice parameters of a and c, and belongs to the space group of C_{6v}^4 or $P6_3mc$. The lattice parameters of the hexagonal unit cells mostly range from 3.2475 to 3.2501 Å for a and from 5.2042 to 5.2075 Å for c [1,2,27]. The density of the ZnO is 5.606 g/cm^3. As shown in Fig. 1, one zinc atom is tetrahedrally coordinated with four oxygen atoms. Such tetrahedral coordination of ZnO gives rise to the noncentrosymmetric structure which is attributed to the piezoelectric nature that is an important property for the fabrication of microelectromechanical systems (MEMS) coupled with sensors, actuators and transducers [28]. Due to the noncentrosymmetric behavior, it also exhibits two polar surfaces on opposite sides and each terminates with the one type of ions only.

When the bonds along the c-direction are from cation (Zn) to anion (O) the polarity is referred to be as Zn polarity, while when the bonds along the c-direction are from anion (O) to the cation (Zn) the polarity is referred to be as oxygen polarity. This polarity is also responsible for a number of properties of ZnO, such as spontaneous polarization and piezoelectricity, and also an important factor in crystal growth, defect generation, plasticity, etching, etc. In addition to polar surfaces, it also has non-polar surfaces. The four most common faces of wurtzite ZnO are the polar Zn-terminated (0001)

†To whom correspondence should be addressed.
E-mail: ybhahn@chonbuk.ac.kr

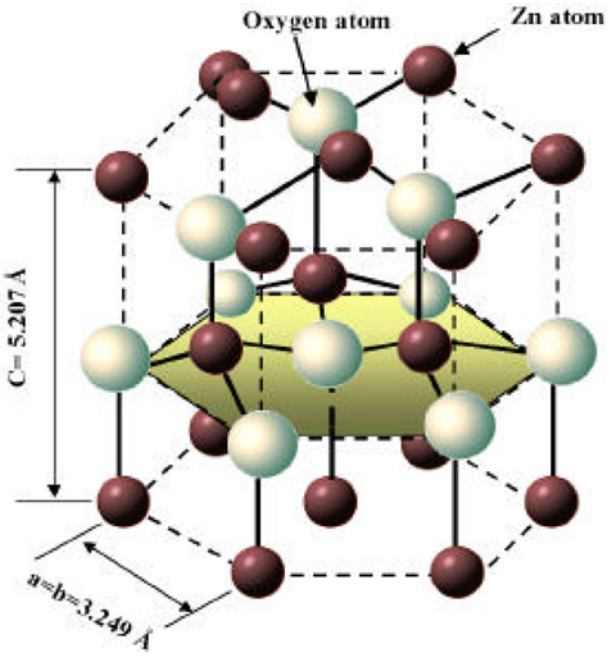

Fig. 1. The hexagonal wurtzite structure model of ZnO. The tetrahedral coordination of Zn-O is shown. O atoms are shown as larger white spheres while the Zn atoms are smaller brown spheres.

and O-terminated (000$\bar{1}$) faces (c-axis oriented), and the non-polar (2$\bar{1}\bar{1}$0) (a-axis) and (01$\bar{1}$0) faces which contain an equal number of Zn and O atoms. It has been observed that the origination of various shapes of the ZnO crystals is due to the relative growth rates of different crystal facets and differences in the growth rates of different crystal planes [29,30]. From an electrostatic point of view, the polar surfaces should not be stable unless charge arrangements and, hence, the opposite ionic charges on the surface result in a spontaneous polarization and normal dipole moment. Furthermore, the polar surfaces and the (01$\bar{1}$0) surfaces are found to be stable; however, the (2$\bar{1}\bar{1}$0) face is less stable and generally has a higher level of surface roughness than its counterparts. In addition, the ZnO has some advantages over GaN which allow for the realization of ZnO-based photonic and optoelectronic devices [31]. Table 1 summarizes the properties comparison between ZnO and GaN [1,2]. Especially, compared to GaN, ZnO has two main advantages over the GaN and GaN-based materials: a larger exciton-binding energy which allows stable emission at room-temperature with high efficiency and lower power threshold for lasing by optical pumping and a feasibility to grow high-quality single crystalline with relatively low cost of GaN.

A DIVERSITY OF ZnO NANOSTRUCTURES AND THEIR STRUCTURAL PROPERTIES

The variety of ZnO nanostructures is dependent on growth mechanism, growth method, synthetic condition, kind of substrate and so on. The nanostructures include nanorods, nanowires, nanocolumns, nanotubes, nanobelts, nanorings, nanoribbons, nanosheet networks, hollow micro- and nano-spheres, nanoflowers, and nanocombs. In this section, typical examples of nanostructures will be reviewed in terms of growth mechanism and structural properties. The structural characterization of as-grown ZnO nanowires was performed by using field emission scanning electron microscopy (FESEM), transmission electron microscope (TEM) and high-resolution TEM equipped ith selected area electron diffraction (SAED) patterns and X-ray diffraction (XRD) pattern which was measured with Cu-Kα radiation. The optical properties were characterized at room-temperature by using Raman-scattering and photoluminescence (PL) spectroscopy, which were measured with the Ar^{+} (513.4 nm) and He-Cd (325 nm) laser line as the exciton sources, respec-

Table 1. Comparison between the properties of wurtzite ZnO and GaN

Properties	ZnO	GaN
Lattice parameters at 300 K		
- a_0 (nm)	0.32495	0.31878
- c_0 (nm)	0.52069	0.51850
- c_0/a_0	1.602	1.627
Density (g/cm^3)	5.606	6.15
Stable phase at 300 K	Wurtzite	Wurtzite
Melting point (°C)	1975	2500
Thermal conductivity (Wcm^{-1} °C^{-1})	0.6, 1-1.2	1.3
Linear expansion coefficient (/°C)	a_0: 6.5 cm$^3\times10^{-6}$	a_0: 5.59 cm$^3\times10^{-6}$
	c_0: 3.0 cm$^3\times10^{-6}$	c_0: 3.17 cm$^3\times10^{-6}$
Static dielectric constant	8.656	8.9
Refractive index	2.008	2.29
Band gap (RT)	3.370 eV	3.390 eV
Band gap (4K)	3.437 eV	3.503 eV
Exciton binding energy (meV)	60	25
Electron effective mass	0.24	0.2
Electron hall mobility at 300 K (cm^2/Vs)	200	<1000
Hole effective mass	0.59	0.8
Hole Hall mobility at 300 K (cm^2/Vs)	5-50	<200

tively.

1. ZnO Nanowires and Nanorods

Nanowires and nanorods are one-dimensional (1D) nanostructures and have received great interest because they have versatile applications such as nanoelectronics devices, photovoltaic systems, chemical and bio sensors. In addition, the 1D nanostructures, owing to their many valuable properties, including a direct band-gap and large exciton binding energy make them a promising candidate for the fabrication of efficient optoelectronic nanodevices. A large number of papers on the synthesis, characteristics, and growth mechanisms of ZnO nanowires and nanorods have been published.

Regarding the growth of the ZnO nanorods/nanowires by gas-phase process, there are two major growth mechanisms reported: vapor-liquid-solid (VLS) [32,33] and vapor-solid (VS) [15-17]. The VLS mechanism is a catalyst-assisted process in which the metal nanoclusters or metal nanoparticles have been used as nucleation sites for the growth of 1D nanostructures. In this process, the gaseous reactants dissolve with the catalytic particles and form alloy-liquid droplets which play an important role in the growth of 1D nanostructures. Precipitation occurs when the liquid droplet becomes supersaturated with the source material and under appropriate gas flow with increasing the time the precipitation increases, which leads to the formation of corresponding 1D structures. There are several metal catalyst components which are used as a catalyst during the growth of 1D nanostructure, such as Au, Sn, Cu, and Co. By contrast, the VS mechanism is a catalyst-free process. It is generally accepted that the control of supersaturation is a key factor to obtain 1D nanostructures because the degree of supersaturation determines the prevailing growth morphology and thus low supersaturation is required for whiskers growth, a medium supersaturation for bulk growth, and high supersaturation for powder growth. In a typical VS process, the source materials are vaporized at a high temperature and then directly condensed onto the substrate placed in the low-temperature region. After the initial condensation, the condensed molecules form the seed crystals which serve as nucleation sites for the further growth of nanostructures. This VS process has been widely used for the growth of various ZnO nanostructures.

Fig. 2(a) shows ZnO nanorods in a high density grown by the catalyst-free VS mechanism. The nanorods are synthesized onto the nickel-coated Si(100) substrate via the thermal evaporation using metallic zinc powder and oxygen at 500-550 °C [36]. The perfectly hexagonal-shaped ZnO nanorods, illustrated in inset of (a), have the Zn-terminated (0001) facets bounded with the $\{01\bar{1}0\}$ surfaces. Fig. 2(b) and (c) show low-magnification TEM and high-resolution TEM (HRTEM) images of the as-grown single ZnO nanorod. The typical diameter of the observed nanorod is ~300 nm with a uniform diameter throughout the length. The HRTEM image exhibits a detailed structural characterization of the as-grown ZnO nanorods, indicating that the as-grown structure is single crystalline with lattice spacing of 0.52 nm, which corresponds to the *d*-spacing of the [0001] crystal planes of the wurtzite ZnO and also confirms the preferential growth direction in the *c*-axis. The corresponding SAED pattern in the inset of (c) obtained from the ZnO nanorod projected along the $[2\bar{1}\bar{1}0]$ zone axis also confirms that the nanorods are single crystalline with the wurtzite hexagonal phase, preferentially grown along the [0001] plane. The crystallinity and crystal phase of the deposited ZnO nanorods were observed by the x-ray diffraction (XRD) pattern in Fig. 2(d). The strong peak of (0002) with a week peak of (0004) indicates that the obtained hexagonal-shaped ZnO nanorods are single crystal with preferential growth along the c-axis direction. Fig. 2(e) shows Raman-scattering spectrum of the as-grown ZnO nanorods, exhibiting sharp, intense and dominated optical-phonon

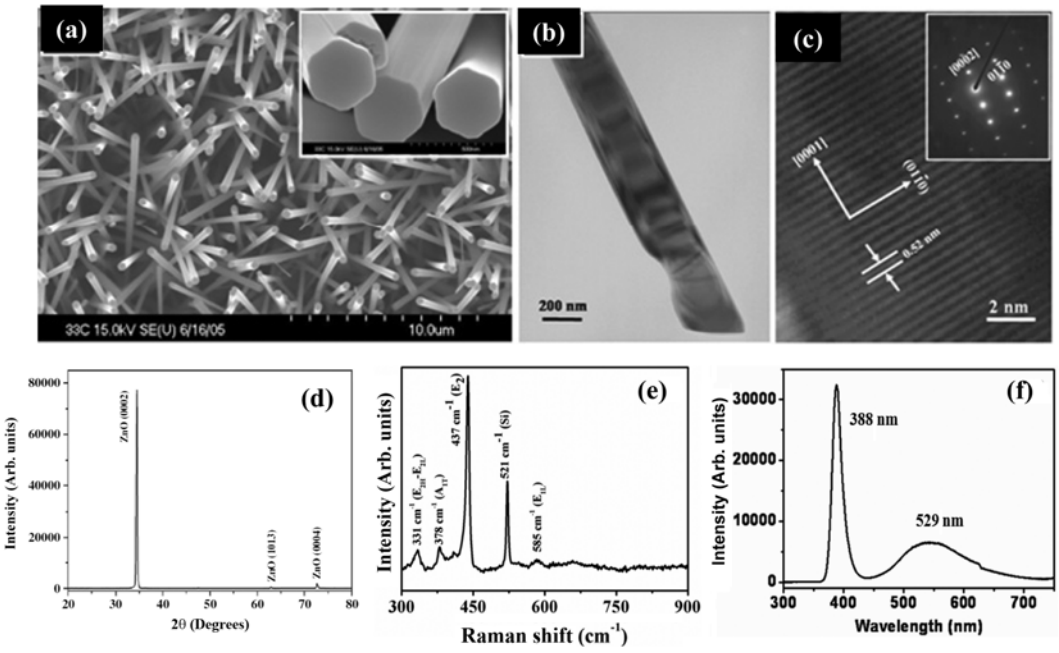

Fig. 2. (a) Low and (inset a) high magnification FESEM images and (b) low and (c) high resolution TEM images and their corresponding SAED pattern (inset of c) of hexagonal-shaped ZnO nanorods grown on nickel-coated Si(100) substrate [36 (a)]. (d) Typical XRD spectrum, (e) Raman scattering, and (f) photoluminescence spectrum measured at room temperature from hexagonal-shaped ZnO nanorods [36 (b)].

E_2 mode and a very small and suppressed E_{1L} mode which indicates that as-grown nanorods are in good crystal quality with the wurtzite hexagonal phase. Fig. 2(f) presents the room-temperature photoluminescence (PL) spectrum measured using a He-Cd laser line of 325 nm as the excitation source. A sharp and strong near-band-edge emission at 388 nm with less significant green emission at 529 nm was observed, which confirms that the as-grown ZnO nanorods have good optical properties with much fewer structural defects.

Fig. 3 shows the hexagonal coaxial-shaped ZnO nanocolumns vertically grown in a high density onto steel alloy substrates via non-catalytic thermal evaporation process using the metallic zinc powder at 490 °C [37]. It is most interesting to observe that the obtained nanocolumns exhibit a coaxial-shaped structure and clearly display a layer-by-layer three-step growth at their top (a). The HRTEM and SAED analysis confirmed that the as-grown nanocolumns were single-crystalline, grown along the [0001] direction (b). To explain the growth process, a three-step growth mechanism has been proposed (c) in which the first step involves the growth of hexagonal rod along the [0001] direction bounded with the six crystallographic equivalent [$01\bar{1}0$] surfaces. As the surface diffusion is the most important rate-limiting process in the ZnO crystal growth, hence the (0001) plane easily disappears and instead it is capped with the lower surface energy facet but higher miller indices of [$01\bar{1}1$] surfaces (step I). After the growth of [$01\bar{1}1$] facet, the (0001) plane was the most likely remaining facet which provides the Zn-terminated (0001) plane which was self-catalytically active and favorable site for the second step growth in the [0001] direction. The nanocolumns were perfectly hexagonal, because of the hexagonal crystallographic feature of the ZnO [107]. Details of the three-step growth mechanism are available elsewhere [37].

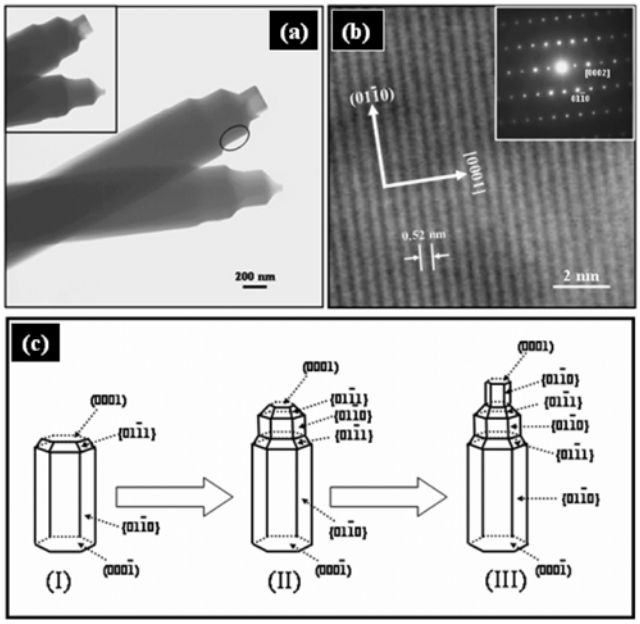

Fig. 3. (a) Low magnified TEM image of the coaxial-shaped ZnO nanocolumns grown on steel alloy, exhibiting a layer-by-layer growth of the nanocolumns. (b) High resolution TEM image observed from the circled portion in (a), showing the single crystallinity, grown along the [0002] direction (inset SAED pattern). (c) Schematic illustration of the three-step growth mechanism for the formation of coaxial-shaped ZnO nanorods [37].

2. ZnO Nanotubes

Fig. 4 shows typical SEM images of ZnO nanotubes (left a-d) grown in solution at low temperature of 65 °C by using zinc nitrate and hexamethylenetetramine [38] and ZnO microtubes (right a-d) synthesized by simple metal-vapor deposition method on NiO particles-coated sapphire substrates using Zn andZnO powders at 950 °C [39]. The FESEM images of the solution-processed ZnO nanotubes having average lengths 1.2±0.2 μm reveal that the nanotubes are grown in a high density, deposited in a partially aligned manner over the whole substrate surface. The nanotubes are exhibiting straight and smooth surfaces throughout their lengths consisting of hollow interiors, indicated by white arrows in (d). The typical diameters and wall thicknesses of the nanotubes are 70±20 nm and 15±5 nm, respectively. By contrast, the metal-vapor deposited ZnO microtubes had hollow-cavity with the perfect hexagonal facets. It was reported that the ZnO microtubes were formed by assembling the several neighboring individual nanowires together in a hexagonal manner and thus forming the microtubes with hexagonal cross sec-

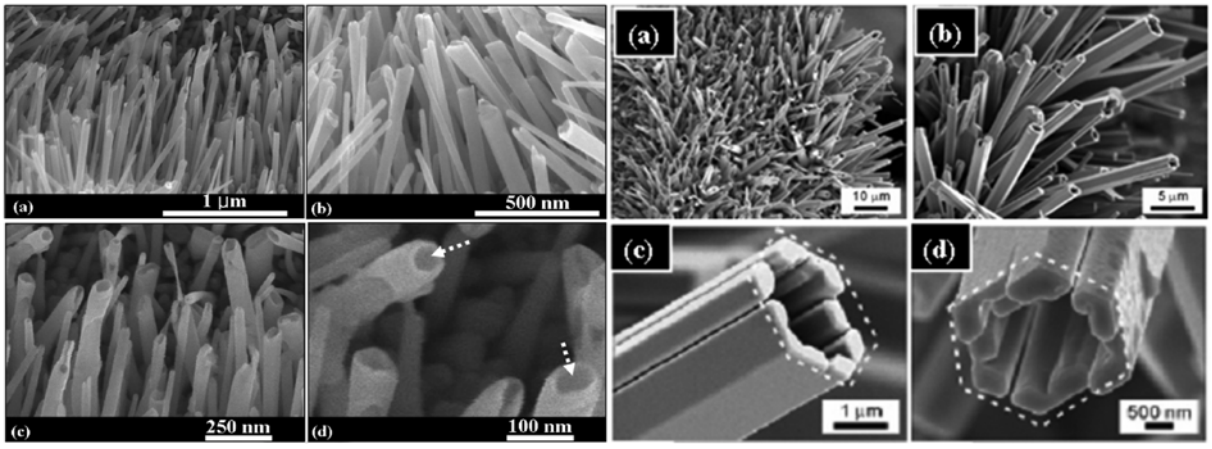

Fig. 4. (Left, a-d) SEM images of ZnO nanotubes (a-d) grown in solution at 65 °C [38]. (Right, a-d) SEM images of ZnO microtubes synthesized by metal-deposition method on NiO-coated sapphire at 950 °C [39].

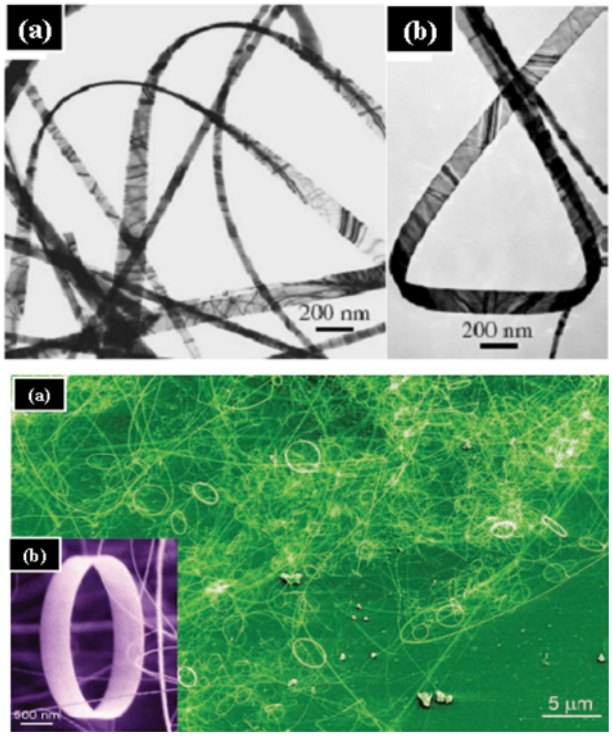

Fig. 5. (Top) Typical TEM images of the ZnO nanobelts by thermal evaporation of ZnO powders at 1,400 °C [42]. (Bottom) (a) Low-magnification TEM image of the as-synthesized ZnO nanorings; and (b) High magnification TEM image of a freestanding single-crystal ZnO nanoring, is showing uniform and perfect geometrical shape [43].

tions [39].

In addition, several research groups reported the growth of ZnO nanotubes by the pyrolysis of zinc acetylacetonate in a two-temperature zone furnace on silicon substrate at 500 °C [40], thermal evaporation using the mixed powders of zinc and zinc oxide onto the silicon substrate at 1,300 °C [41], metal organic chemical vapor deposition process using the diethyl zinc and oxygen as source materials for zinc and oxygen at 350-450 °C [42], etc.

3. ZnO Nanobelts and Nanorings

Fig. 5 shows the nanobelts (top) grown by thermal evaporation using high purity ZnO powders as source material at 1,400 °C for 2 h [42] and the free-standing ZnO nanorings (bottom) by an epitaxial self-coiling of polar nanobelts using the mixture of ZnO, indium oxide and lithium carbonate powders in the weight ratio of 20 : 1 : 1 at 1,400 °C and 10^{-3} Torr in a horizontal quartz tube furnace for 30 min [43]. All the nanobelts (top of Fig. 5) have uniform width passim to their length with the length of several tens to several hundreds of micrometers, showing clean and atomically sharp surfaces of the nanobelts without any sheathed amorphous phase. A vapor-solid growth process was proposed for the formation of the as-grown ZnO nanobelts. These structures were grown along the [0001] direction, enclosed by ± $(2\bar{1}\bar{1}0)$ and ± $(01\bar{1}0)$, showing no defects or dislocations [42]. Large-scale synthesis of ZnO nanobelts in an aligned fashion has been performed via the thermal evaporation process using metallic zinc plates at 450±10 °C under ambient pressure for 3-5 h under constant flow of argon. The structural characterizations by XRD and HRTEM revealed that the as-grown products are single-crystalline with wurtzite structure and mostly grow along the [0001] direction. Wen et al. also presented the fabrication of ZnO nanobelts arrays directly from and on zinc substrates in a horizontal quartz tube furnace using the metallic zinc powder-coated zinc foil substrates at 600 °C for 6 h [44]. They proposed a gas-solid tip growth mechanism, different from the typical VLS mechanism, for the as-grown nanobelts in which the atomic diffusion in the solid was a rate-determining step.

For the synthesis of free-standing ZnO nanorings (bottom of Fig. 5), the decomposition of ZnO into Zn^{2+} and O^{2-} was the key step for controlling the anisotropic growth of nanobelts. SEM image revealed that the as-formed nanorings had a perfect circular shape of the complete rings with uniform shapes and flat surfaces, having 1-4 μm of diameter and 10-30 nm thickness of thin and wide shells. Detailed structural examination by HRTEM and SAED exhibited that the nanobelts had a growth direction of [$10\bar{1}0$], while the side surfaces were ± (1-210), and top/bottom surfaces ± (0001). Details of formation of such nanorings are available elsewhere [43].

4. Hollow ZnO Nano- and Micro-spheres

Fig. 6 shows the growth of ZnO nanospheres and micro-sized hollow spheres/cages (top) [45] and polyhedral cages of ZnO (bottom) [130]. The ZnO nanospheres and micro-sized hollow spheres/cages were synthesized on Si(100) and steel alloy substrates in a high density via the thermal evaporation using different zinc precursors, i.e., $ZnCl_2$ and metallic zinc powder in the presence of oxygen. It is worthwhile to note that the ZnO microcages/spheres grown onto the Si(100) substrate surface present smooth and clean outer surfaces, while the growth of small ZnO nanowires containing the small metal particles at their tips was also observed from outer and inner surfaces of the structures grown onto the steel alloy substrates (inset in b). It was also observed that uniformly deposited

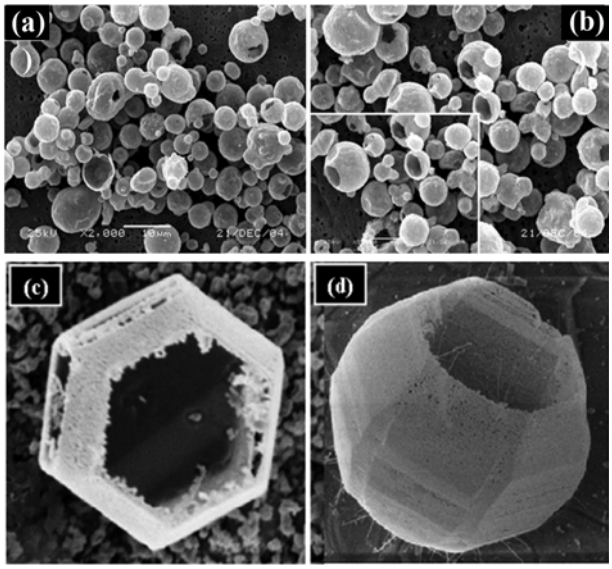

Fig. 6. (Top) SEM images of ZnO microcages/spheres grown onto the Si(100) (a) and steel alloy substrates (b), respectively synthesized by thermal evaporation of metallic zinc powders [45]. (Bottom) SEM images of single-crystalline polyhedral cages and shells of ZnO [46].

ZnO nanospheres had been synthesized onto the Si(100) substrates at 500-700 °C using zinc chloride ($ZnCl_2$) and oxygen. Although not illustrated, Raman scattering analysis showed a characteristic ZnO wurtzite hexagonal peak at 436.9 cm^{-1} in case of Si(100) substrate, while at 437 cm^{-1} in case of steel alloy substrate. The room-temperature PL spectra in both the cases showed a broad band in the visible region with suppressed and short UV emission, indicating that these structures had some structural defects such as zinc interstitials and oxygen vacancies [45]. Polyhedral cages and shells were formed on alumina substrates via the solid-vapor deposition process using the commercial ZnO, SnO_2 and graphite powders at 1,100 °C [46]. The walls of the cages/shells were composed of mesoporous and textured ZnO nanocrystals. A possible growth mechanism for the formation of the ZnO cages/spheres was proposed which involved the solidification of zinc liquid droplets in the form of single-crystalline spherical and hexagonal-based rod zinc particles, surface oxidation which produce the textured ZnO nanocrystals on the zinc surfaces and finally the vaporization or sublimation of the zinc cores, which results the formation of ZnO cage/shell structures [46]. The detailed characterizations combined with the growth mechanism of zinc oxide microcages were reported by Fan et al. [47], who synthesized these structures using the zinc powder and oxygen at 800 °C on the silicon substrates. They proposed a growth process that includes the deposition of the zinc polyhedral particles, breaking of top {0001} surfaces of the zinc polyhedral particles because of oxidation by the residual oxygen or water vapors. Finally, sublimation of zinc through the broken holes of the top {0001} faces leads to the formation of cage-like structures. In this synthesis, initially grown single-crystal zinc polyhedral crystals served as templates for the growth of the ZnO cages.

5. Star- and Flower-shaped ZnO Nanostructures

Fig. 7 shows the star-shaped ZnO onto the Au-coated Si(100) substrate at 450 °C (top) [48] and the flower-shaped on Si(100) and Si(111) substrates 400-500 °C [49], both by the cyclic feeding chemical vapor deposition (CFCVD) using the diethyl zinc (DEZn) and O_2 as zinc and oxygen sources, respectively. The star-shaped ZnO nanostructures consist of triangular-shaped blades: sharpened tips with wider bases. The wider bases of each blade are joined to each other at one center and form the multipod star-shaped morphology. Interestingly, it was observed that the upper portion of these structures exhibited perfectly hexagonal cones (top a, b). The room-temperature PL spectra from the as-grown samples exhibited a narrow ultraviolet emission with a broad and strong green emission. However, by annealing the as-grown samples in an oxygen atmosphere at 500 °C for 30 min, reversibly a sharp and strong UV emission with a suppressed green emission was observed, which confirmed that fewer oxygen vacancies exist after annealing. The flower-shaped ZnO nanostructures grown on Si(100) and Si(111) substrates without the use of metal catalyst or additives exhibited triangular shaped leaves, rooted in one center. The typical length of one leaf in a flower-shaped structure on Si(100) is about 300-400 nm, while the diameters at the bases and tips are in the ranges 100-130 nm and 40-60 nm, respectively (bottom a). These structures are formed by the deposition of many layers, and each layer contains several leaves which are joined to each other through their wider bases. The flower-shaped structures grown onto the Si(111) substrate contain uniform leaves with the hexagonal faceted (bottom b). It is interesting to note that the obtained leaves are similar to small ZnO nanorods with uniform diameter passim to their length, originating from one center. The appearance of different morphologies on the different orientations of the silicon substrates is probably due to the dissimilar interactions at ZnO-substrate interface [49]. The flower-shaped structures show a sharp and strong UV emission band at 378 nm and a suppressed and broad green emission band at 520 nm in the visible region.

6. Other Morphologies of ZnO

Different other morphologies of ZnO nanostructure are also reported in literature. He et al. reported the growth of ZnO nanotetra-

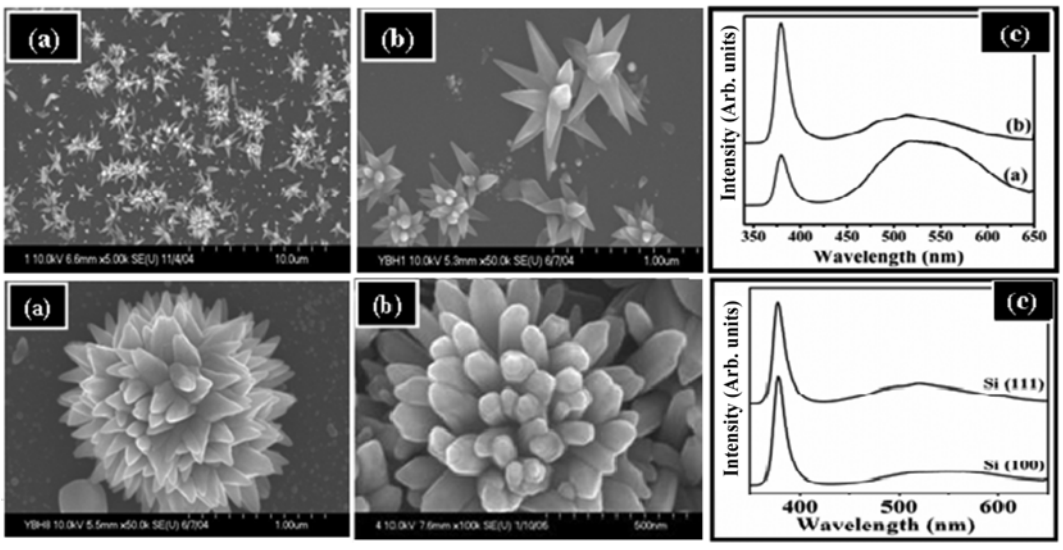

Fig. 7. (Top) Typical star-shaped ZnO nanostructures: (a) low and (b) high magnification FESEM images and (c) PL spectra measured from multipod star-shaped ZnO nanostructures grown at 450 °C by the cyclic feeding chemical vapor deposition on Au coated Si (100) substrate [48]. (Bottom) Typical flower-shaped ZnO nanostructures grown at 400-500 °C by the cyclic feeding chemical vapor deposition on (a) Si (100) and (b) Si(111) substrates and PL spectra, respectively [49].

pods with hexagonal crowns by the non-catalytic vapor-transport method using the high purity zinc powder in oxygen on silicon at 630 °C [50]. They exhibited the synthesis of uniform tetrapod-like ZnO nanostructures in bulk quantity by the thermal evaporation using metallic zinc powder at 850-925 °C [51]. The as-synthesized nanostructures were single crystalline with the wurtzite hexagonal phase having the lattice constants of a=0.324 nm and c=0.519 nm. Wang et al. reported comb-like ZnO nanostructures and their growth for the first time [52]. It was observed that the Zn-terminated ZnO (0001) polar surface was chemically active while the oxygen terminated (0001) polar surface was inert during the growth of nanocantilever arrays. They observed that relatively longer and wider "comb like" nanocantilever arrays were grown from the Zn-terminated (0001) surfaces by a self-catalyzing growth process due to the enrichment of Zn at the growth front. Unlikely, the oxygen-terminated (0001) surfaces which are chemically inactive, cannot initiate any growth. Yan et al. synthesized high-yield of microscale comb-like structures made of periodic arrays of single-crystalline ZnO nanowires by chemical vapor transport and condensation method using metallic zinc powder at 800-900 °C on silicon substrate [53]. They observed that the comb-like structures were grown onto the substrate more than 90%. Gao et al. reported the synthesis of the polar-surface-dominated ZnO nanopropeller arrays via a two-step high-temperature VS mechanism using the mixtures of ZnO, SnO_2 and graphite powders, first at 1,200 °C for 60 min and then 1,300 °C for 30 min on polycrystalline Al_2O_3 substrate [54].

DEVICES APPLICATIONS OF ZnO NANOSTRUCTURES

1. ZnO Nanowire-based Field Effect Transistors

A one-dimensional ZnO nanostructure is a good building block for the fabrication of high-performance electronic and photonic devices. ZnO is intrinsically an n-type semiconductor, mainly due to the presence of oxygen vacancies and zinc interstitials. Field-effect transistors (FETs) which are good for understanding the electronic properties of the single ZnO nanowire or nanorod are fabricated by a number of groups [55]. A conventional approach to fabricate the FETs is the random dispersion of nanowires from nanowires-containing solution, followed by metallization at the known nanostructure location on substrates using conventional electron beam lithography (EBL). To fabricate such type of FETs, typically, first the nanowires are separated from the substrate by scratching and sonicating in ethanol and/or isopropyl alcohol and then transferred onto a substrate. The patterns for the electrical contacts are fabricated by the EBL onto a selected individual ZnO nanowire and metal layers are deposited sequentially onto the contact area by electron beam evaporation. The electrical measurements of the fabricated ZnO nanowires-based FETs are generally performed using 4-probe station (HP 4156C semiconductor parameter analyzer) in the range from 20 fA to 100 mA at room temperature.

Fig. 8 shows the schematic of a typical single ZnO nanowire-based bottom-gate and top-gate FETs and the drain current *vs*. drain-source voltage (I_{DS}–V_{DS}) for electrical characteristics of the fabricated back-gate (a) and top-gate FETs which were annealed at 450 °C under a flow of O_2 for 2 min [56]. As seen from m the I_{DS}–V_{DS} characteristics of the fabricated back- and top-gate FETs measured at different gate voltages (Vg), with increasing the V_{DS}, the I_{DS} is also increasing significantly, which is typical for *n*-type FETs. The currents at the gate bias of 12 V for the single ZnO nanowire based FETs fabricated by applying back- and top-gate approaches were observed ~006 μA and 1.24 μA, respectively which indicates that the top-gate FET show higher current performance as compared to the single nanowire FET fabricated by back-gate approach. However, the conventional fabrication methods described above have some limitations: the limited current drive per single nanowire and low throughput and processing complexity because of integrating nanowires within the device channel by a physical arrangement method.

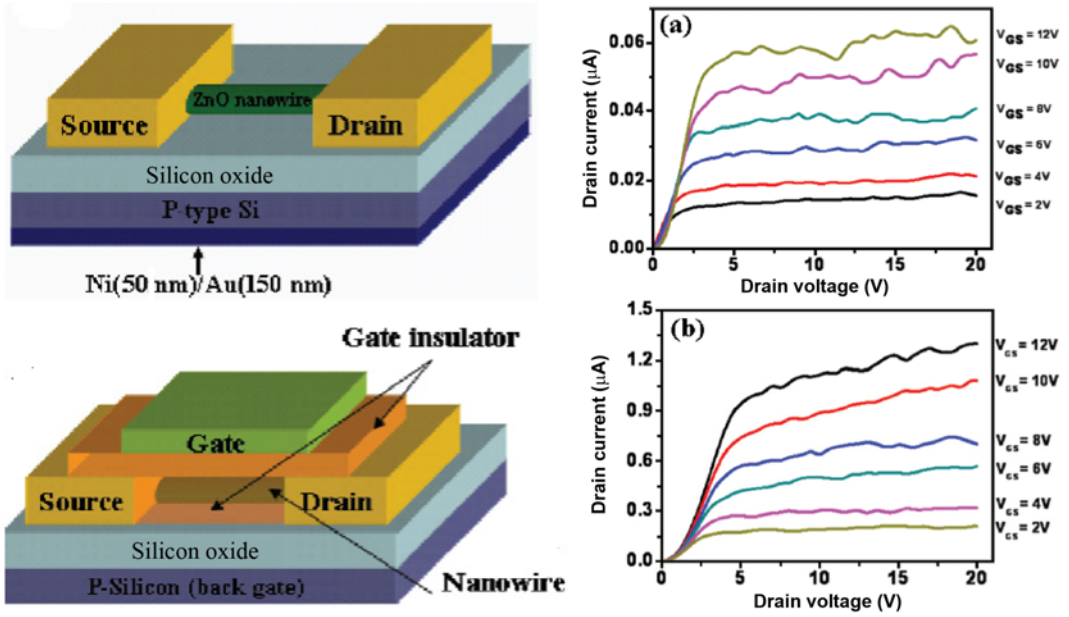

Fig. 8. (Left) Schematic illustration of bottom- and top-gate FETs, (right) drain current - drain-source voltage curves for the bottom-gate FET (a) and top-gate FET (b), respectively [56].

Furthermore, with such method it is not easy to control the number of nanowires and to properly align them between electrodes, and thus not ideal for economical integration. Hence, for practical device applications of ZnO nanostructures, it is crucial to grow them selectively on wanted areas of substrate either in vertical or horizontal direction.

The vertical growth of ZnO nanowires (or nanorods) on substrates has been achieved by various methods such as vapor-liquid-solid growth with metal catalysis [57], nanosphere-masking lithography [58], photolithography [59] electron-beam lithography [60]. However, compared to the vertical growth the lateral growth of ZnO nanowires is rather difficult. Methods for the lateral growth are reported for the metal-catalyst-prepattern assisted selective growth [61], the seed-layer assisted selective growth by the use of ZnO films or nanoparticles [62], the lateral overgrowth of nanowires arrays onto [2-1-10] surface of single crystal ZnO substrate by combining the electron-beam lithography and the hydrothermal decomposition method [63,64], and the catalyst-free direct growth of nanobridges on prefabricated trenched electrodes by thermal evaporation [65]. However, as shown in Fig. 9 such methods resulted in the vertical growth components, complex structural networks, the intersection of nanowires in the middle between electrodes, the sparse growth of nanowires with poor lateral alignment, and the use of expensive single-crystalline ZnO substrates which all should be removed for device performance. Another issue for the nanowire-based transistors is how to obtain relatively high on-current and how to adjust the drive current capability of the device [66].

To solve such problems, Hahn et al. demonstrated a hybrid method for the lateral growth of multiple ZnO nanorods between electrodes in solution without the use of metal catalyst [67]. This method enables one to directly align a number of nanowires between electrodes with or without intersection in the middle and to completely eliminate the vertical growth components and complex structural networks. They named the FETs fabricated with the overlapped and the overlap-free ZnO nanorods as '*Type 1 FET*' and '*Type 2 FET*', respectively. Fig. 10 shows high magnification FESEM images of *Type 1* and *Type 2* FETs (left), logarithmic and linear (inset) scale

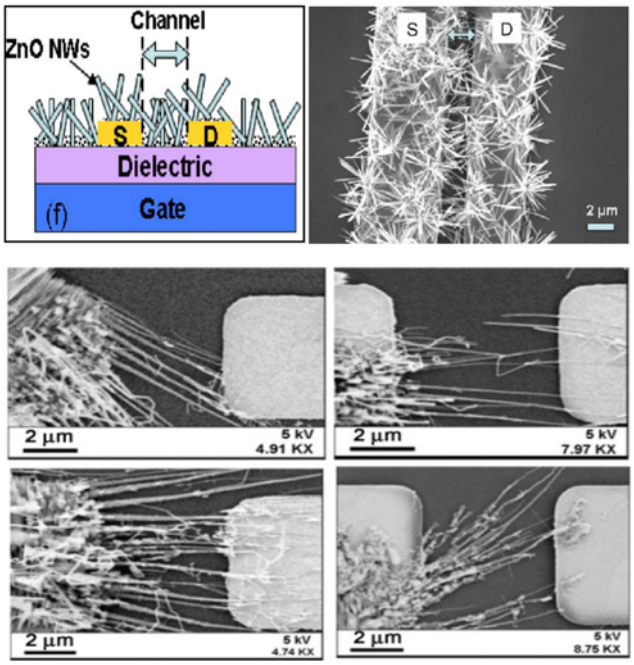

Fig. 9. (Top) Schematic diagram and SEM image of ZnO nanowire FET structure on polymer substrate [64 (a)]. (Bottom) ZnO nanowires bridged between electrodes [64 (b)].

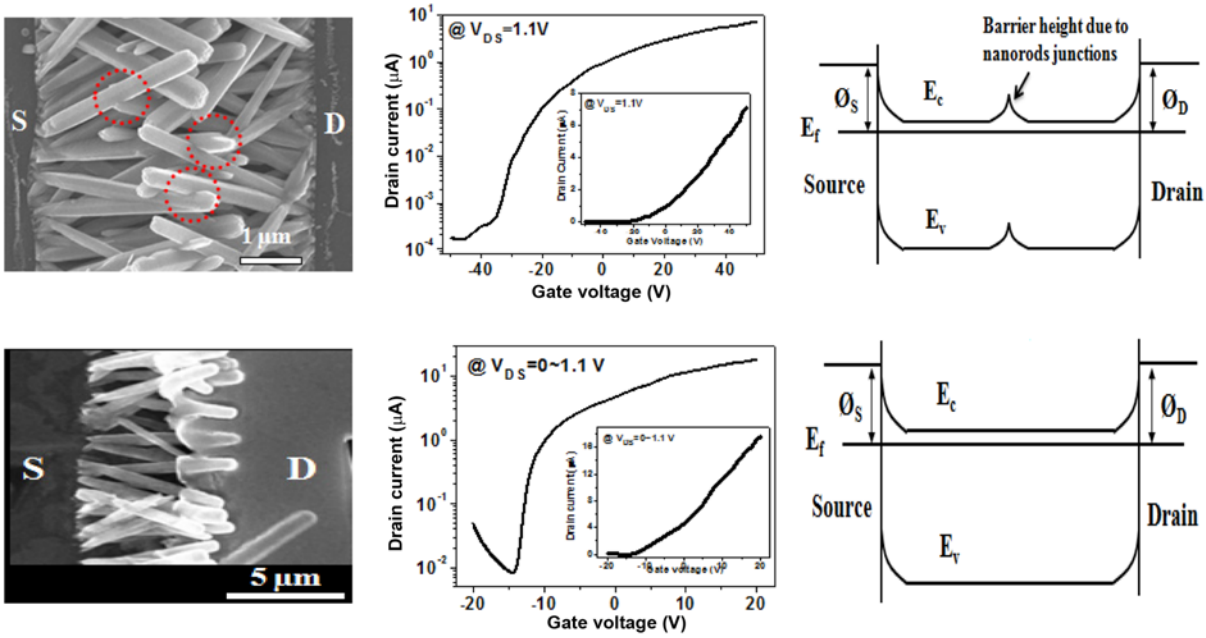

Fig. 10. (Left) SEM top views of '*Type 1*' and 'Type 2' *FETs* fabricated with overlapped and overlap-free ZnO nanorods between electrodes. (Middle) Drain current-voltage characteristic curves measured from '*Type 1*' and 'Type 2' *FETs* with logarithmic and linear (inset) scale drain-current vs. gate-voltage curve at V_{DS}=1.1 V. (Right) Energy band diagrams across electrodes for '*Type 1 FET*' with overlapped ZnO nanorods (a) and '*Type 2 FET*' with overlap-free ZnO nanorods (b) [67].

drain current versus gate-voltage curves at V_{DS}=1.1 V (middle), and energy band diagrams across electrodes for *Type 1* and *Type 2* FETs (right), respectively. The overlap-free ZnO nanorods *Type 2* FETs showed better performance with mobility of ~8.5 $cm^2V^{-1}s^{-1}$ and on/off ratio of ~4×10^5 than the overlapped ZnO nanorods *Type 1* FETs having mobility of ~5.3 $cm^2V^{-1}s^{-1}$ and on/off ratio of ~3×10^4. All the FETs fabricated in this work showed much better performance than the previously reported solution-based ZnO FETs. As in the laterally-grown ZnO nanorods FETs, the nanorod networks provide multiple conducting paths for electrons but also substantially influence the electron transport at the nanorods junctions and nanorod-metal junctions; the electron transport behavior in *Type 1 FET* is substantially influenced by the nanorods junctions in the middle. Hence, as shown in Fig. 10 (right), the barrier height of the overlapped nanorods is greater than that of overlap-free nanorods. Hahn et al. reported the effective barrier heights of 0.45 eV and 0.36 eV for *Type 1* and *Type 2 FETs*, respectively [67].

2. Four-probe Electrode System Based on ZnO Nanorod Arrays Directly Grown in Solution

The conventional approach to fabricating nanowire FETs, described in the previous section 1, is not ideal for the economical integration of nanodevices. Thus, instead of randomly placing nanowires or nanorods on a substrate, a more desirable method would be appreciated to selectively grow and pattern nanostructures directly onto electrodes or other wanted areas of the substrate. Details of solution-based growth methods are available elsewhere [60,72]. As shown in Fig. 11, Hahn et al. proposed a method for growing aligned ZnO nanorod arrays directly on a four-point probe structure in solution at low temperatures (<100 °C) and measuring the electrical characteristics of the four-point electrode system [60 (b)]. This method enabled them to perform electrical measurements directly on the as-grown ZnO nanorod arrays without any additional processing. In addition, they investigated the hydrogen sensing properties using the ZnO aligned nanorod arrays four-point probe, exhibiting an increase in the sensitivity with increasing the concentration of H_2 and the operating temperature.

3. Pattern-controlled Growth of Vertically-aligned ZnO Nanorods Arrays and their Application for Field-emission Devices

A selective area growth of well-aligned ZnO nanostructures is crucial for devices applications of 1D nanostructures and thus various techniques like nanosphere lithography [68], polystyrene microsphere based self-assembly monolayers [69], silane-based self-assembled monolayers [70], and conventional photolithography [71] have been reported. However, such methods, except conventional photolithography, require relatively high temperature, expensive mask, complex multi-step processes, and metal catalysts in some cases. To solve such a drawback of the photolithography and grow ZnO nanostructures selectively on pre-patterned substrates, we proposed the hybrid approach of combining electron-beam lithography (top-down) and solution growth method (bottom-up) [72]. Fig. 12 (left) shows the low and high magnification FESEM images of ZnO nanorod arrays grown selectively on pre-patterned Si substrates with diameters of 2 μm (a, b), 500 nm (c), and 50~100 nm (d), respectively. Fig. 12 (right) presents field emission current density vs. electric field plot for selectively grown spherical-shaped ZnO nanorod arrays with showing a uniform florescent field emission (inset, a) and corresponding Fowler-Nordheim plot (b). The hybrid approach used in this work produced an excellent control of periodicity, location, and density of ZnO nanorod arrays on the substrates. The field emission measurements from the as-grown ZnO nanorod arrays showed low turn-on field of ~2.85V/μm and high field-enhancement factor (β) of ~1.68×10^3. Details are available elsewhere [72].

4. ZnO Nanorods Based Heterojunction Devices

ZnO is a promising material to replace GaN for solid light-emit-

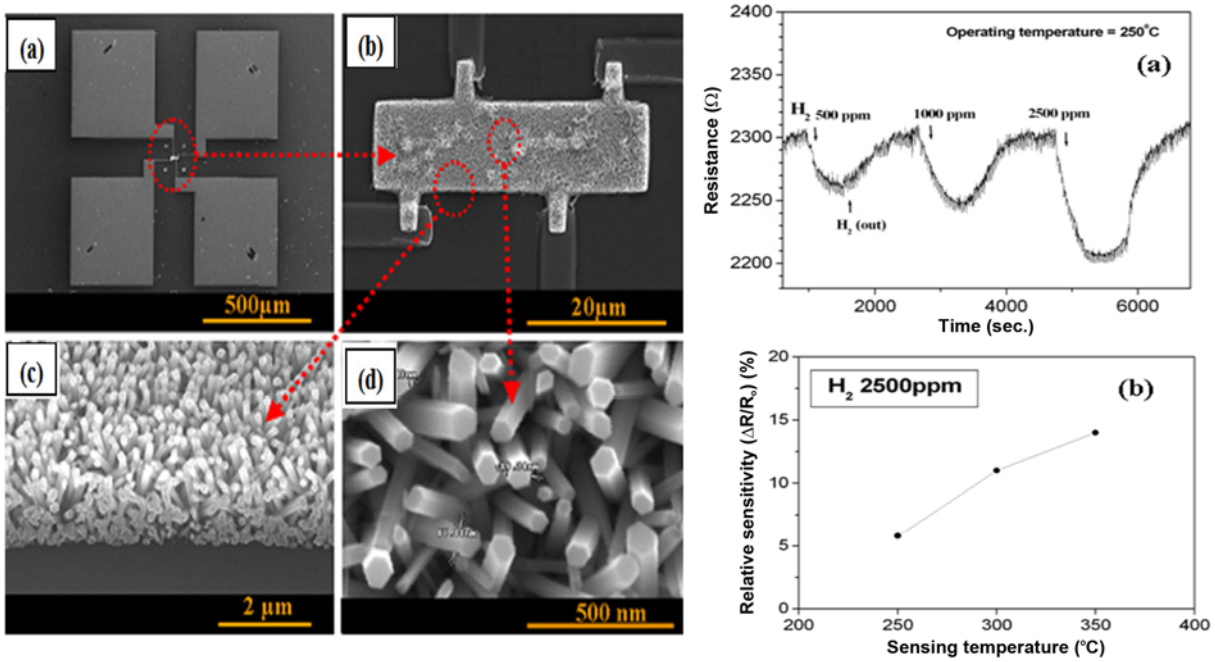

Fig. 11. (Left, a-d) FESEM images of ZnO nanorod arrays directly and selectively grown on a fourpoint probe structure. (Right) (a) Dynamic responses of the patterned ZnO nanorod arrays to H_2 pulses at 250 °C and (b) sensitivity at various operating temperatures [60 (b)].

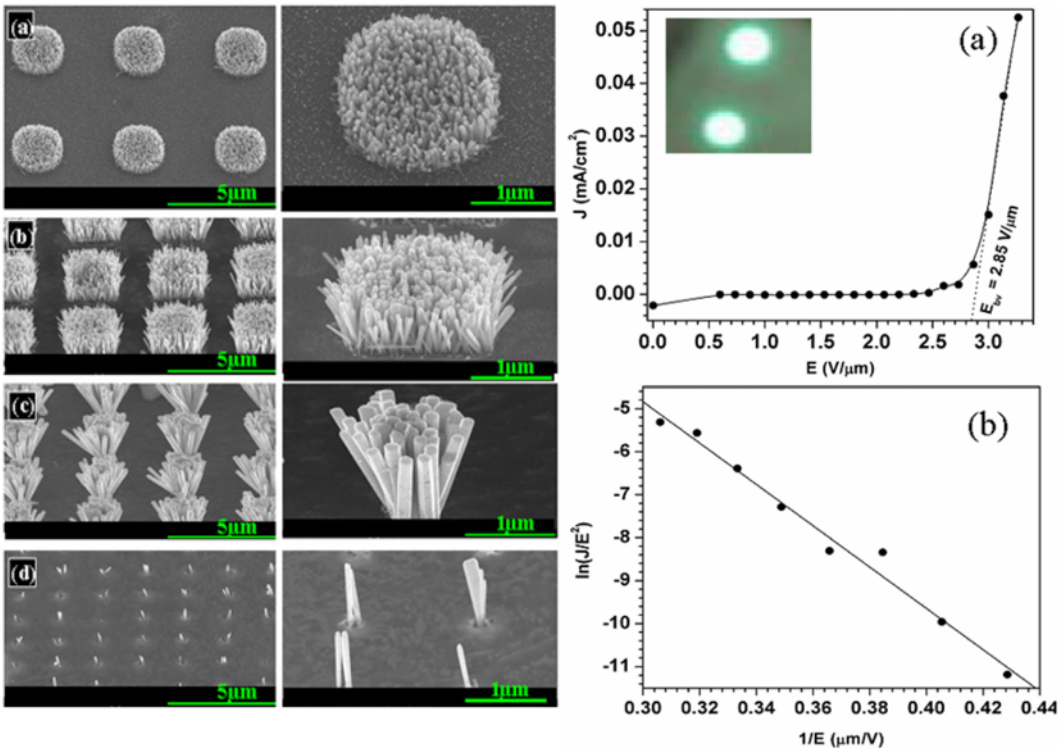

Fig. 12. (Left, a-d) Typical FESEM images of ZnO nanorod arrays grown selectively on pre-patterned Si substrates. (Right, a-b) Field emission current density versus electric field plot for selectively grown spherically shaped ZnO nanorod arrays: inset in (a) shows a uniform fluorescent field emission, and (b) corresponding F-N (Fowler and Nordheim) plot [72].

ting diodes (LEDs). However, a few papers reported on the growth of high quality *n*-type ZnO films on *p*-GaN or vice versa. [73] No work has been reported on the growth of well-aligned ZnO nanorods using a simple and economic solution method on *p*-GaN layers and the temperature-dependent device performance of *n*-ZnO nanorods. We reported the synthesis and characterization of well-aligned ZnO nanorods grown on *p*-type GaN/Al_2O_3 substrate in the area of 0.3-1.5 cm^2 in solution as described elsewhere [74] and the performance of *p*-*n* junction diode (*n*-ZnO nanorods/*p*-GaN) studied at different temperatures. Fig. 13 shows the schematic of the *n*-ZnO nanorods/*p*-GaN diode structure and the SEM image of ZnO nanorods on p-GaN substrate in solution [75], which shows the nanorods uniformly grown along the vertical orientation, i.e., [0001] *c*-axis direction. Fig. 14 (left) shows the I-V plots of In/ZnO nanorods measured at different temperatures (20-150 °C) (a) and the surface structures of ZnO nanorods (b). The I-V plots present good ohmic behavior of In contacts with ZnO nanorods at all temperatures [76]. At room temperature, the as-grown ZnO nanorods on GaN exhibited an electrical resistance of ~10 Ω, while increasing temperature the resistance of In/ZnO nanorod structures increased exponentially from ~10 to 12 Ω. Fig. 14 (right) shows the temperature-dependent heterojunction behavior of *n*-ZnO nanorods/*p*-GaN diode with I-V measurements at different temperatures (20-150 °C) under dark condition (a). At all temperatures, the device exhibited an excellent rectifying behavior, with the rectification factor (I_F/I_R) of 2880 at a bias voltage of ~2 V at room temperature. The ln(J) vs. ln(V) plots of *p*-*n* diode for two different temperatures of 20 and 150 °C exhibit three distinct regions in the voltage range of <1.5 V (region-I), between 1.5 and 2.5 V (region-II), and >2.5 V (region-III). These three regions are attributed to a field emission or tunneling mechanism to recombination-tunneling mechanism, recombination-tunneling mechanism, and space-charge-limited current conduction of monocarriers, respectively.

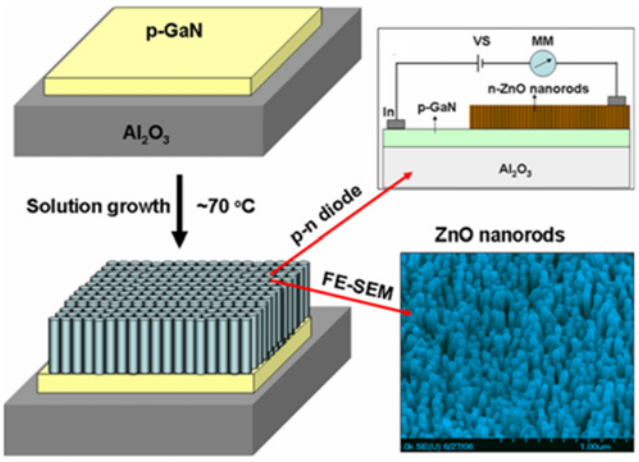

Fig. 13. Schematic diagrams of the *n*-ZnO nanorods/*p*-GaN diode structure and the SEM image of ZnO nanorods on p-GaN substrate in solution [75].

5. ZnO Nanowires Based Solar Cells

Due to wide bandgap (3.37 eV) and high electron affinitiy (4.25 eV), the ZnO is an attractive material for solar energy harvesting devices. The electron mobilities are much higher in ZnO than TiO_2, while the conduction band edge of both materials is located at ap-

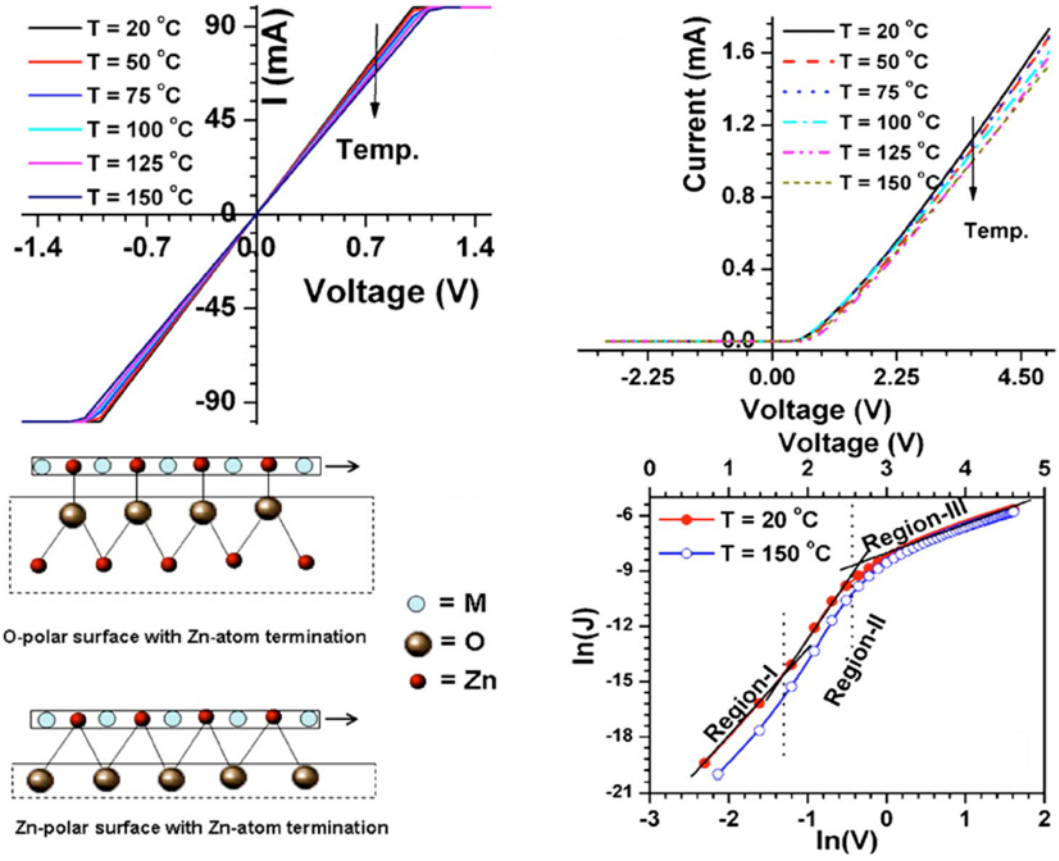

Fig. 14. (Left) I-V plots of In/ZnO structures grown on GaN/Al_2O_3 substrates at different temperatures and surface structures of ZnO nanorods. (Right) Current-voltage plots and ln(J) vs. ln(V) plots of *n*-ZnO nanorods/*p*-GaN heterojunction device at different temperatures [75].

proximately the same level. Therefore, nanostructured ZnO could be a good candidate as electron acceptor and transport material in hybrid solar cells including dye-sensitized solar cells (DSSCs). Keis et al. reported the fabrication of DSSCs using nanostructured ZnO particles and obtained 5% efficiency [77]. Kakiuchi et al. presented the fabrication of DSSCs by applying nanostructured ZnO films and obtained an efficiency of ~4.1% under AM-1.5 illumination at 100 mW/cm^2 [78]. Aydil et al. fabricated a DSSC using branched ZnO nanowires grown by MOCVD using the zinc acetylacetonate hydrate and oxygen as source materials for zinc and oxygen, respectively, on conductive glass substrate (F : SnO_2) at 550 °C [79]. The as-obtained dendrite-like branched nanowires enhanced the surface areas and provided a direct conduction path for electrons between the point of photogeneration and the conducting substrate, and thus improved electron transport compared to films of sintered nanoparticles. The DSSC based on the nanowires-branched ZnO exhibited energy conversion efficiencies of 0.5% with internal quantum efficiencies of 70%. Yang et al. also fabricated ZnO nanowires-based DSSCs [80], as shown in Fig. 15 (top) which shows the schematic of the ZnO nanowire arrays into ruthenium based dye-sensitized solar cells (a), the ZnO nanowire arrays grown onto the fluorinated tin oxide (FTO) substrates using the aqueous solutions of zinc nitrate hydrate, hexamethylenetetramine and polyethylenimine at 92 °C for 50 h (b). Fig. 15 (middle, c) shows the plots of current density *vs.* bias voltage for two cells with different active areas of 0.2 cm^2 (small cell) and 0.8 cm^2 (large cell). The small cell shows a higher short circuit current J_{sc} and open circuit voltage V_{oc} than the large cell. Fig. 15 (middle, d) presents a performance comparison of nanowire- and nanoparticle-based cells. They observed that the TiO_2 films showed a higher current than either of the ZnO films and a larger initial slope than the small ZnO particles, consistent with better transport through TiO_2 particle networks. Ko et al. reported a high efficiency DSSC fabricated using ZnO nanoforest composed of high density, long branched tree-like hierarchical ZnO nanostructures [81]. Fig. 15 (bottom) shows the schematic structure and J-V curve of DSSC with nanoforest ZnO NWs. They concluded that the overall light-conversion efficiency was almost five times higher than that of DSSCs based on vertically-grown ZnO nanowires.

6. Nanogenerators Based on Piezoelectric ZnO Nanowires

Recently, Wang et al. presented a very novel and innovative approach to convert nanoscale mechanical energy into electrical energy by utilizing piezoelectric ZnO nanowires [82-84]. Fig. 16 (top) shows the piezoelectric power generation using p-ZnO nanowire arrays grown on (001) Si via thermal vapor deposition method [83]. They recorded three-dimensional plots of the output voltage at an external load. The measurements were performed by the AFM using Si tips coated with Pt film, with a cone angle of 70°. The operation mechanism of the power nanogenerator relies on the coupling of piezoelectric and semiconducting properties of ZnO as well as the formation of Schottky barrier between the metal and ZnO contacts.

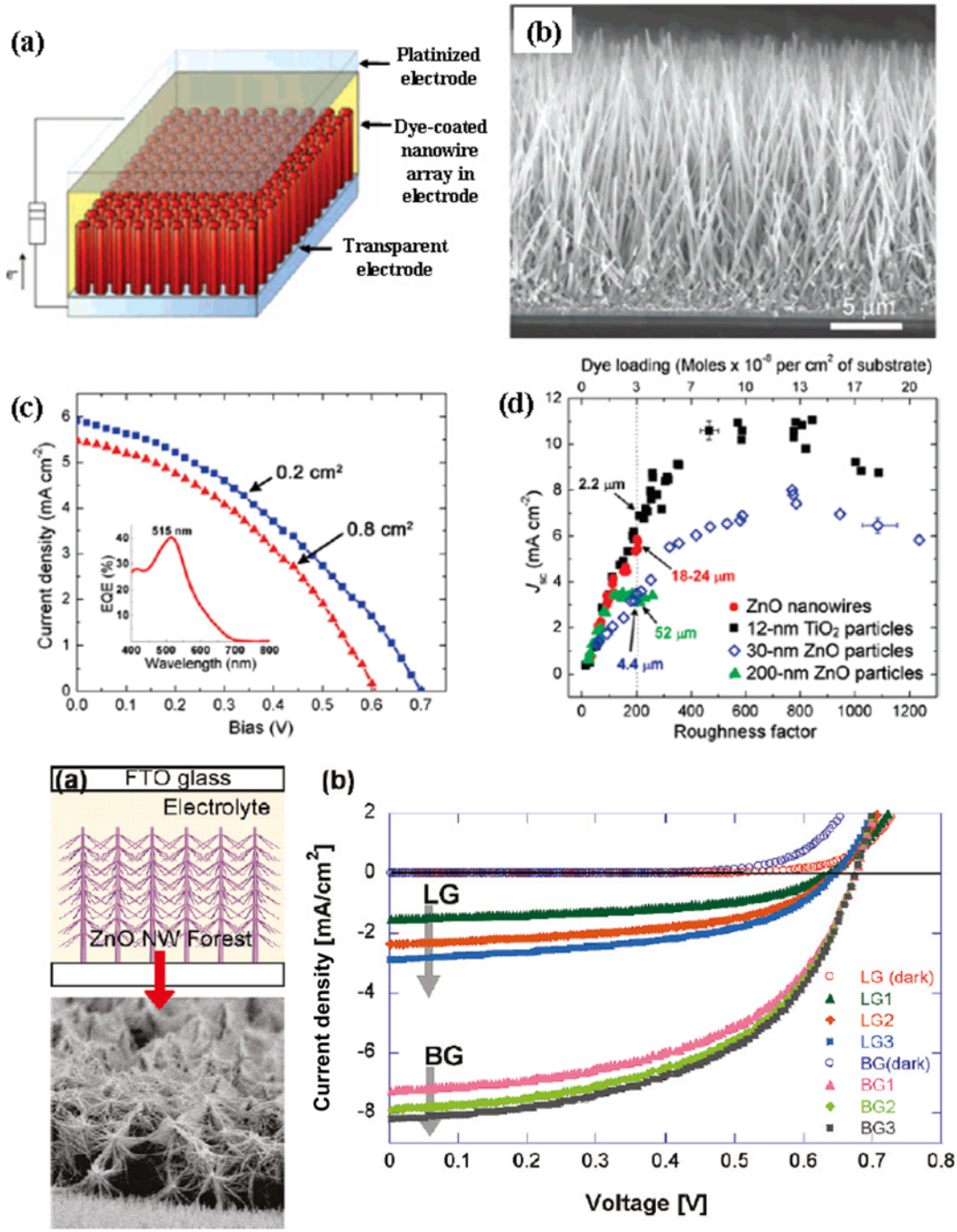

Fig. 15. (Top) Schematic diagram of DSSC based on ZnO nanowire arrays, (Middle) Current density versus voltage (J-V) for a small cell (active area, 0.2 cm^2; efficiency of 1.51%) and a large cell (0.8 cm^2; 1.26%). Inset: EQE versus wavelength for the large cell. Comparative performance of nanowire and nanoparticle cells in terms of short-circuit current density (J_{SC}) versus roughness factor for cells based on ZnO nanowires, 12-nm TiO_2 particles, and 30- and 200-nm ZnO particles. Cell size: 0.8 cm^2 [80]. (Bottom) Schematic structure and SEM image of nano-forest ZnO nanowires, and J-V curve for the DSSC based on nano-forest ZnO nanowires [81].

Fig. 16 (top, right) illustrates the model for understanding the electricity output characteristics of the p-ZnO nanowire. The model explains that where the piezoelectric charges are partially screened by free carriers having a relatively low-doping level, the presence of a Schottky barrier between the AFM tip and NW is required to rectify the flow of charge carriers. As a result, the current can only flow in the direction along which the Schottky barrier is at forward bias. For a metal-p-type semiconductor contact, the Schottky barrier at the interface is at forward bias if the semiconductor has a higher potential, otherwise it is reversely biased. Details are available elsewhere [83]. They also fabricated a flexible high-output nanogenerator (HONG) based on laterally-grown ZnO nanowire arrays [84]; its schematic structure and demonstration of the output scaling-up are shown in Fig. 16 (bottom, a and b) with the open circuit voltage

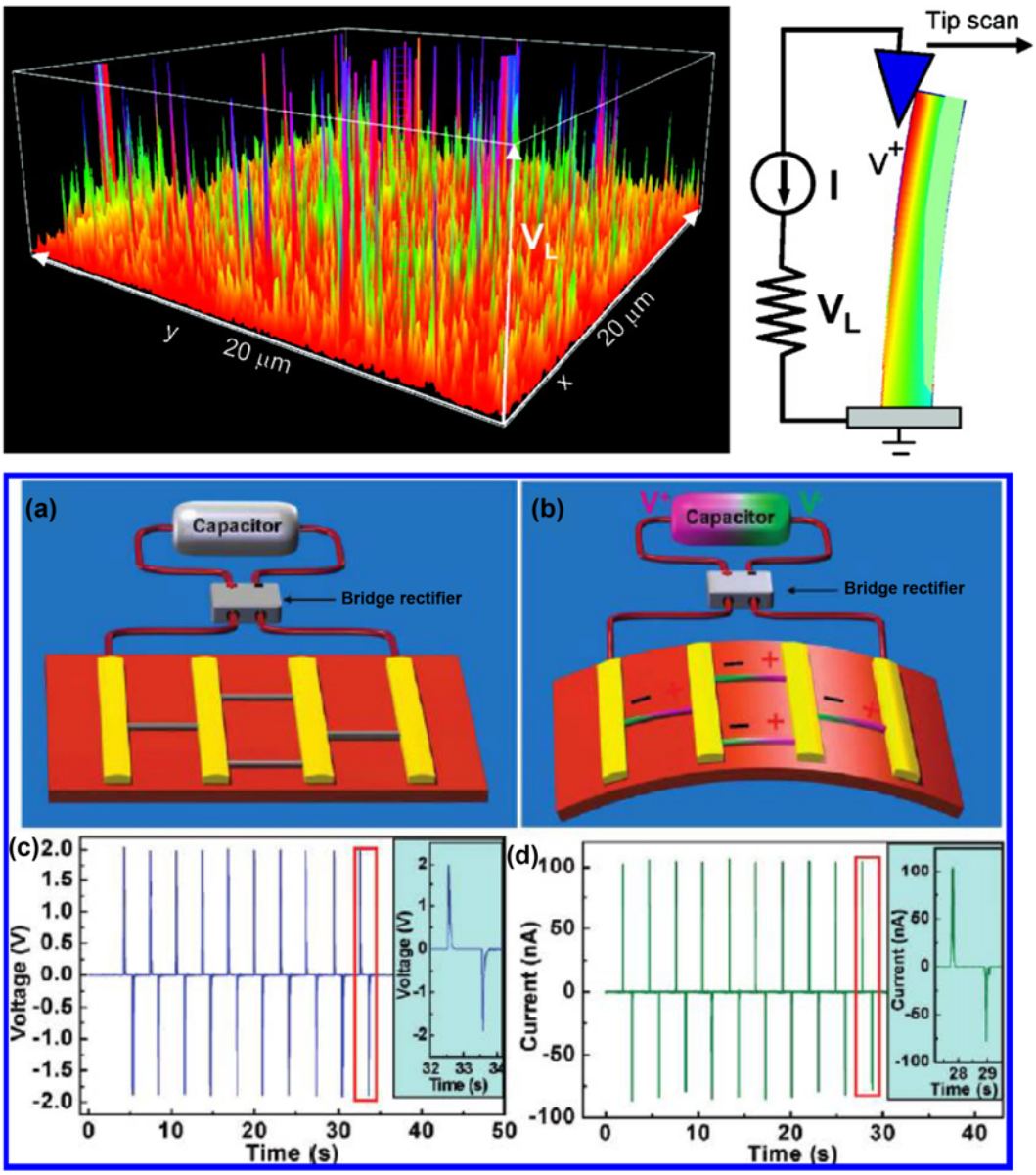

Fig. 16. (Top) (a) Output voltage from the piezoelectric power generator using p-type vertically-grown ZnO nanowires and schematic for understanding the electricity output characteristics of the p-ZnO nanowire [83]. (Bottom) Schematic diagram of HONG's structure without mechanical deformation in which gold is used for Schottky contacts with ZnO nanowires and (b) Demonstration of output scaling-up when mechanical deformation is induced. (c) Open-circuit voltage and (d) Short-circuit current measurements of HONG [84].

(c) and short circuit current (d) of the HONG which were measured at a strain of 0.1% and strain rate of 5% per second with the deformation frequency of 0.33 Hz. Using a single layer of HONG structure, they obtained an open-circuit voltage of up to 2.03 V and a peak output power density of ~11 mW/cm^3.

7. ZnO Nanostructures Based Glucose and Chorlesterol Biosensors

As the 1D ZnO nanostructures have high electron affinity and high-surface to volume ratio of one-dimension nanostructures, they can be used for the fabrication of electrical sensors, electrochemical biosensors. Umar et al. also reported a glucose biosensor fabricated with well-crystallized ZnO nanonails grown by thermal evaporation process at ~650 °C [85]. They used the ZnO nanonails as supporting matrixes for glucose oxidase (GOx) immobilization to construct an efficient glucose biosensor (Nafion/GOx/ZnO/Au). The GOx immobilized on the surfaces of ZnO nanonails had more spatial freedom in its orientation, which facilitated the direct electron transfer between the active sites and electrode surface. Fig. 17 shows a schematic diagram of chorlesterol (or glucose) biosensor (top) and a typical steady-state amperometric response of the ZnO nanonails-modified glucose biosensor on successive addition of glucose in the 0.01 M PBS solution (pH 7.4) at an applied potential of 0.8 V (a) and the Lineweaver-Burk plot of 1/i vs 1/C (c). The biosensor exhibited a rapid and sensitive response to the change of glucose concentration. With subsequent addition of glucose to the stirring, the phosphate buffer showed a decrease in the reduction current.

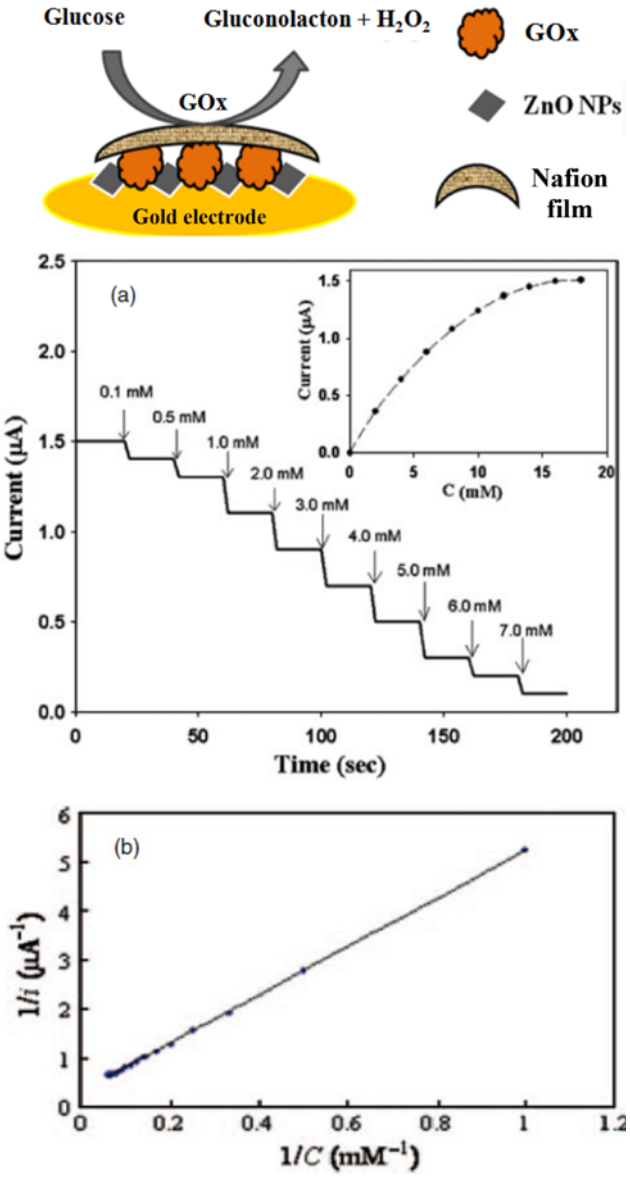

Fig. 17. (Top) Schematic diagram for understanding the ZnO nanorods-based glucose biosensor. (Middle) Amperometric response of Nafion/ZnO nanorods/Au electrode with successive addition of glucose to the 0.01 M PBS buffer solution (pH=7.4). The applied potential was +0.8 V (vs Ag/AgCl (sat'd KCl) reference). (Bottom) Lineweaver-Burk plot of 1/i vs 1/C [85].

The time required for the 95% steady-state response was less than 5 s, indicating a good electrocatalytic and fast electron exchange behavior of the GOx/ZnO nanonails electrode. Inset in (a) shows the corresponding calibration curve of the fabricated glucose sensor, exhibiting an increase in response current with the glucose concentration with reaching a saturated value at a high concentration. The linear calibration range from 0.1 to 7.1 mM with a correlation coefficient of R=0.9937 showed that the fabricated glucose biosensor had a high sensitivity of 24.613 μA/cm^{2}mM. The detection limit of the glucose was 5 μM, much less than the previously reported ZnO-based glucose sensors. Although not illustrated, we examined nanoparticles and flower-shaped nanostructures of ZnO for chorlesterol detection: the former showed a sensitivity of 23.7 μA/cm^{2}μM, detection limit of 3.7×10^{-4} mM [86], and the latter exhibited showed a sensitivity of 61.7 μA/cm^{2}μM and detection limit of 0.012 μM [87], respectively. The higher sensitivity with the flower-shaped ZnO is attributed to greater surface areas than those of nanoparticles.

CONCLUSIONS

The synthesis of ZnO nanostructures and their applications are reviewed in terms of growth method, characteristics, and devices. The zinc oxide has a great diversity in structural morphology, probably the richest family of nanostructures among all materials, which thus lead the publication of thousands of research papers and hundreds of patents. The device applications of ZnO nanostructures include field effect transistors, field-emission devices, piezoelectric nanogenerators, biosensors, p-n heterjunction diodes such as light-emitting diodes and photovoltaic cells, and so on. A low-cost and easy technique needs to be developed by which a specially-wanted shape of nanostructure can be synthesized. Especially, the patterning and selective growth of ZnO nanostructures on desired sites are very important for the nanodevices fabrications and integrations. The growth of p-type ZnO nanostructures and fabrication of p-n junction into a single nanostructure for the fabrication of electrically driven nanodevices is needed to be researched. In addition, as the ZnO is a biocompatible and biosafe, the functionalization of ZnO nanomaterials for bio applications is also promising these days. At last but not least, the future directions for study on ZnO nanostructures are seemingly boundless, but will obviously are driven by demand for the successful achievements of devices.

ACKNOWLEDGEMENTS

This work was supported in part by the Pioneer Research program (2009-0082837) and by the World Class University program (R31-2008-000-10100-0), and the Priority Research Centers Program (2010-0029707) through the National Research Foundation of Korea funded by the Ministry of Education, Science and Technology (MEST). Authors also thank KBSI, Jeonju branch for taking good quality SEM and TEM images, respectively.

REFERENCES

1. *Handbook of Semiconductor Nanostructures and Nanodevices*, Edited by A. A. Balandin and K. L. Wang, American Scientific Publishers (2005), *Encyclopedia of Nanoscience and Nanotechnology*, Edited by H. S. Nalwa, American Scientific Publishers (2011).
2. *Metal Oxide Nanostructures and Their Applications*, Edited by Ahmad Umar and Yoon-Bong Hahn, American Scientific Publishers (2010).
3. S. Chen, Y. Liu, C. Shao, R. Mu, Y, Lu, J. Zhang, D. Shen and X. Fan, *Adv. Mater.*, **17**, 586 (2005); K. Hara, T. Horiguchi, T. Kinoshita, K. Sayams, H. Sugihara and H. Arakawa, *Sol. Energy Mater. Sol. Cells*, **64**, 115 (2000).
4. B. Pal and M. Sharon, *Mater. Chem. Phys.*, **76**, 82 (2002).
5. J. Q. Xu, Q. Y. Pan, Y. A. Shun and Z. Z. Tian, *Sens. Actua. B: Chem.*, **66**, 277 (2000).

6. P. M. Martin, M. S. Good, J. W. Johnston, L. J. Bond and S. L. Crawford, *Thin Solid Films*, **379**, 253 (2000); S. Lee, Y. H. Im and Y. B. Hahn, *Korean J. Chem. Eng*., **22**, 334 (2025).
7. S. Muthukumar, C. R. Golra, N. W. Emanetoglu, S. Liang and Y. J. Lu, *J. Cryst. Growth*, **225**, 197 (2001).
8. S. C. Minne, S. R. Manalis and C. F. Quate, *Appl. Phys. Lett*., **67**, 3918 (1995).
9. K. Keis, L. Vayssieres, S. Lindquist and A. Hagfeldt, *Nanostuct. Mater*., **12**, 487 (1999).
10. C. R. Golra, N. W. Emanetoglu, S. Liang, W. E. Mayo, Y. Lu, M. Wraback and H. J. Shen, *Appl. Phys*., **85**, 2595 (1999).
11. Z. L. Wang, *Mater. Today*, 26 (2004).
12. S. J. Pearton, D. P. Norton, K. Ip, Y. W. Heo and T. Steiner, *Superlatt. Microstruct.*, **34**, 3 (2003).
13. T. Zhang, W. Dong, M. K. Brewer, S. Konar, R. N. Njabon and Z. R. Tian, *J. Am. Chem. Soc*., **128**, 10960 (2006).
14. G. C. Yi, C. Wang and W. II Park, *Semicond. Sci. Technol*., **20**, S22 (2005).
15. A. Eftekhari, F. Molaei and H. Arami, *Mater. Sci. Eng. A*, **437**, 446 (2006).
16. G. Shen, J. H. Cho, J. K. Yoo, G. C. Yi and C. J. Lee, *J. Phys. Chem. B*., **109**, 5491 (2005).
17. G. Shen, D. Chen and C. J. Lee, *J. Phys. Chem. B*., **110**, 15689 (2006).
18. B. P. Zhang, N. T. Binh, K. Wakatsuki, Y. Segawa, Y. Yamada, N. Usami, M. Kawasaki and H. Koinuma, *Appl. Phys. Lett*., **84**, 4098 (2004).
19. J. Liu, P. X. Gao, W. J. Mai, C. S. Lao, Z. L. Wang and R. Tummala, *Appl. Phys. Lett.*, **89**, 63125 (2006).
20. J. Y. Lao, J. Y. Huang, D. Z. Wang and Z. F. Ren, *Nano Lett.*, **3**, 235 (2003); J. Y. Lao, J. G. Wen and Z. F. Ren, *Nano Lett.*, **2**, 1287 (2002); F. Liu, P. J. Cao, H. R. Zhang, J. Q. Li and H. J. Gao, *Nanotechnology*, **15**, 949 (2004); X. Y. Kong, Y. Ding, R. S. Yang and Z. L. Wang, *Science*, **303**, 1348 (2004); P. Gao and Z. L. Wang, *J. Phys. Chem. B*., **106**, 12653 (2002); Y. Liang, X. Zhang, L. Qin, E. Zhang, H. Gao and Z. Zhang, *J. Phys. Chem. B.*, **110**, 21593 (2006); A. Umar, S. Lee, Y. S. Lee, K. S. Nahm and Y. B. Hahn, *J. Cryst. Growth*, **277**, 479 (2005).
21. A. Sekar, S. H. Kim, A. Umar and Y. B. Hahn, *J. Cryst. Growth*, **277**, 471 (2005); A. Umar, S. H. Kim, Y. S. Lee, K. S. Nahm and Y. B. Hahn, *J. Cryst. Growth*, **282**, 131 (2005); A. Umar and Y. B. Hahn, *Nanotechnology*, **17**, 2174 (2006); A. Umar, H. W. Ra, J. P. Jeong, E.-K. Suh and Y. B. Hahn, *Korean J. Chem. Eng*., **23**, 499 (2006); A. Umar, J. P. Jeong, E. K. Suh and Y. H. Hahn, *Korean J. Chem. Eng*., **23**, 860 (2006).
22. W. I. Park, D. H. Kim, S. W. Jung and G. C. Yi, *Appl. Phys. Lett*., **80**, 4232 (2002); W. Lee, H. G. Sohn and J. M. Myoung, *Mater. Sci. Forum*, **449**, 1245 (2004); B. P. Zhang, N. T. Binh, Y. Segawa, K. Wakatsuki and N. Usami, *Appl. Phys. Lett*., **83**, 1635 (2003); S. Lee, A. Umar, S. H. Kim, N. K. Reddy and Y. B. Hahn, *Korean J. Chem. Eng*., **24**, 1084 (2007).
23. R. Kaur, A. V. Singh, K. Sehrawat, N. C. Mehra and R. M. Mehra, *J. Non-Cryst. Sol*., **352**, 23, 2565 (2006); Y. W. Chen, Y. C. Liu and S. X. Lu, *J. Chem. Phys*., **123**, 134701 (2005); A. Dev, S. K. Panda, S. Kar, S. Chakrabarti and S. Chaudhuri, *J. Phys. Chem. B*, **110**, 14266 (2006).
24. B. Cao, Y. Li, G. Duan and W. Cai, *Cryst. Growth Design*, **6**, 1091 (2006); X. Wu, G. Lu, C. Li and G. Shi, *Nanotechnology*, **17**, 4936 (2006).
25. B. Liu and H. C. Zeng, *J. Am. Chem. Soc.*, **125**, 4430 (2003); J. M. Wang and L. Gao, *J. Mater. Chem*., **13**, 2551 (2003); M. Guo, P. Diao and S. M. Cai, *J. Solid State Chem*., **178**, 1864 (2005); S. Kar, A. Dev and S. Chaudhuri, *J. Phys. Chem. B.*, **110**, 17848 (2006); T. Ghoshal, S. Kar and S. Chaudhuri, *J. Cryst. Growth*, **293**, 438 (2006).
26. C. K. Xu, G. D. Xu, Y. K. Liu and G. H. Wang, *Solid State Commun*., **122**, 175 (2002); X. Gao, X. Li and W. Yu, *J. Phys. Chem. B.*, **109**, 1155 (2005); H. Zhang, D. Yang, D. Li, X. Ma, S. Li and D. Que, *Cryst. Growth Des.*, **5**, 547 (2005).
27. R. R. Reeber, *J. Appl. Phys.*, **41**, 5063 (1970).
28. A. Kuoni, R. Holzherr, M. Boillat and N. F. de Rooij, *J. Micromech. Microeng*., **13**, S103 (2003); F. R. Blom, D. J. Yntema, F. C. M. Van de Pol, M. Elwenspoek, J. H. J. Fluitman and Th. J. A. Popma, *Sens. Actuators A-Phys*., **A21**, 226 (1990).
29. O. Dulub, L. A. Boatner and U. Diebold, *Surf. Sci*., **519**, 201 (2002).
30. W. J. Li, E. W. Shi, W. Z. Zhong and Z. W. Yin, *J. Cryst. Growth*, **203**, 186 (1999); J. C. Phillips, *Bonds and Bands in Semiconductors*, Academic Press, New York (1973).
31. Y. Segawa, A. Ohtomo, M. Kawasaki, H. Koinuma, Z. K. Tang, P. Yu and G. K. L. Wong, *Phys. Stat. Sol*., **202**, 669 (1997).
32. (a) R. S. Wagner and W. C. Ellis, *Appl. Phys. Lett*., **4**, 89 (1964). (b) R. S. Wagner, W. C. Ellis, S. M. Arnold and K. A. Jackson, *J. Appl. Phys*., **35**, 2993 (1964).
33. Y. Wu and P. Yang, *J. Am. Chem. Soc*., **123**, 3165 (2001); S. Y. Bae, H. W. Seo and J. H. Park, *J. Phys. Chem. B*., **108**, 5206 (2004).
34. P. Chang, Z. Fan, W. Tseng, D. Wang, W. Chiou, J. Hong and J. G. Lu, *Chem. Mater.*, **16**, 5133 (2004); M. H. Huang, Y. Wu, H. Feick, N. Tran, E. Weber and P. Yang, *Adv. Mater.*, **13**, 113 (2001); Q. X. Zhao, M. Millander, R. E. Morjan, Q.-H. Hu and E. E. B. Campbell, *Appl. Phys. Lett.*, **83**, 165 (2003); Z. Fan, D. Wang, P. Chang, W. Tseng and J. G. Lu, *Appl. Phys. Lett*., **85**, 5923 (2004).
35. J. H. He, J. H. Hsu, C. H. Wang, H. N. Lin, L. J. Chen and Z. L. Wang, *J. Phys. Chem. B.*, **110**, 50 (2006); X. Y. Kong and Z. L. Wang, *Nano Lett.*, **3**, 1625 (2003); P. X. Gao, Y. Ding and Z. L. Wang, *Nano Lett.*, **3**, 1315 (2003).
36. (a) A. Umar, B. Karunagran, E. K. Suh and Y. B. Hahn, *Nanotechnology*, **17**, 4072 (2006); (b) A. Umar, S. H. Kim, J. H. Kim and Y. B. Hahn, *J. Nanosci. Nanotechnol.*, **7**, 4522 (2007).
37. A. Umar and Y. B. Hahn, *Appl. Phys. Lett*., **88**, 173120 (2006).
38. Y. K. Park, A. Umar, S. H. Kim and Y.-B. Hahn, *J. Nanosci. Nanotechol*., 7, 6349 (2008).
39. J. S. Jeong, J. Y. Lee, J. H. Cho, H. J. Suh and C. J. Lee, *Chem. Mater.*, **17**, 2752 (2005).
40. J. J. Wu, S. C. Liu, C. T. Wu, K. H. Chen and L. C. Chen, *Appl. Phys. Lett*., **81**, 1312 (2002).
41. Y. J. Xing, Z. H. Xi, Z. Q. Xue, X. D. Zhang, J. H. Song, R. M. Wang, J. Xu, Y. Song, S. L. Zhang and D. P. Yu, *Appl. Phys. Lett*., **83**, 1689 (2003).
42. Z. L. Wang, *J. Phys.: Condens. Matter*, **16**, R82 (2004).
43. X. Y. Kong, Y. Ding, R. Yang and Z. L. Wang, *Science*, **303**, 1348 (2004).
44. X. Wen, Y. Fang, Q. Peng, C. Yang, J. Wang, W. Ge, K. S. Wong and S. Yang, *J. Phys. Chem. B*, **109**, 15303 (2005).
45. A. Umar, S. H. Kim, Y. H. Im and Y. B. Hahn, *Superlattices and Microstructures*, **39**, 238 (2006).
46. P. X. Gao and Z. L. Wang, *J. Am. Chem. Soc*., **125**, 11299 (2003).

47. H. J. Fan, R. Scholz, F. M. Kolb, M. Zacharias and U. Gosele, *Sol. State Commun*., **130**, 517 (2004).
48. A. Umar, S. Lee, Y. S. Lee, K. S. Nahm and Y. B. Hahn, *J. Cryst. Growth*, **277**, 479 (2005).
49. A. Umar, S. Lee, Y. H. Im and Y. B. Hahn, *Nanotechnology*, **16**, 2462 (2005).
50. F. Q. He and Y. P. Zhao, *App. Phys. Lett.*, **88**, 193113 (2006).
51. Y. Dai, Y. Zhang, Q. K. Li and C. W. Nan, *Chem. Phys. Lett*., **358**, 83 (2002).
52. Z. L. Wang, X. Y. Kong and J. M. Zuo, *Phys. Rev. Lett.*, **91**, 185502 (2003).
53. H. Yan, R. He, J. Johnson, M. Law, R. J. Saykally and P. Yang, *J. Am. Chem. Soc.*, **125**, 4728 (2003).
54. P. X. Gao and Z. L. Wang, *Appl. Phys. Lett.*, **84**, 2883 (2004).
55. G. Shen, Y. Bando and C. J. Lee, *J. Phys. Chem. B*., **109**, 10779 (2005); M. S. Arnold, P. Avouris, Z. W. Pan and Z. L. Wang, *J. Phys. Chem. B*, **107**, 659 (2003); P. C. Chang, Z. Fan, D. Wang, W.-Y. Tseng, W.-A. Chiou, J. Hong and J. G. Lu, *Chem. Mater.*, **16**, 5133 (2004); Z. Fan, D. Wang, P. C. Chang, W. Y. Tseng and J. G. Lu, *Appl. Phys. Lett*., **85**, 5923 (2004); J. Y. Park, Y. S. Yun, Y. S. Hong, H. Oh, J. J. Kim and S. S. Kim, *Appl. Phys. Lett.*, **87**, 123108 (2005); J. Y. Park, H. Oh, J. J. Kim and S. S. Kim, *Nanotechnology*, **17**, 1255 (2006); (a) Y. S. Yun, Y. Y. Park, H. Oh, J. J. Kim and S. S. Kim, *J. Mater. Res*., **21**, 132 (2006), (b) Y. W. Heo, L. C. Tien, D. P. Norton, B. S. Kang, F. Ren, B. P. Gila and S. J. Pearton, *Appl. Phys. Lett.*, **85**, 2002 (2004); J. Y. Park, H. Oh, J. J. Kim and S. S. Kim, *J. Cryst. Growth*, **287**, 145 (2006); J. Goldberger, D. J. Sirbuly, M. Law and P. Yang, *J. Phys. Chem. B*., **109**, 9 (2005); W. I. Park, J. S. Kim, G.-C. Yi, M. H. Bae and H.-J. Lee, *Appl. Phys. Lett*., **85**, 5052 (2004); (a) W. Q. Yang, H. B. Huo, L. Dai, R. M. Ma, S. F. Liu, G. Z. Ran, B. Shen, C. L. Lin and G. G. Qin, *Nanotechnology*, **17**, 4868 (2006); (b) A. Umar, B.-K. Kim, J.-J. Kim and Y. B. Hahn, *Nanotechnology*, **18**, 175606 (2007).
56. Y. K. Park, A. Umar, S. H. Kim, J.-H. Kim, E. W. Lee, M. Vaseem and Y. B. Hahn, *J. Nanosci. Nanotechnol*., **8**, 6010 (2008).
57. H. T. Ng, J. Li, M. K. Smith, P. Ngnuyen, A. Cassell, J. Han and M. Meyyappan, *Science*, **300**, 1249 (2003).
58. X. D. Wang, C. J. Summers and Z. L. Wang, *Nano Lett*., **4**, 423 (2004).
59. D. F. Liu, Y. J. Xiang, X. C. Wu, Z. X. Zhang, L. F. Liu, L. Song, X. W. Zhao, S. D. Luo, W. J. Ma, J. Shen, W. Y. Zhou, G. Wang, C. Y. Wang and S. S. Xie, *Nano Lett*., **6**, 2375 (2006**)**.
60. (a) Q. Ahsanulhaq, S. H. Kim and Y. B. Hahn, *J. Alloys and Compounds*, **484**, 17 (2009); (b) Q. Ahsanulhaq, J. H. Kim, J. S. Lee and Y. B. Hahn, *Electrochem. Commun*., **12**, 475 (2010).
61. W. I. Park, C. H. Lee, J. H. Chae, D. H. Lee and G. C. Yi, *Small*, **5**, 181 (2009); P. X. Gao, J. Liu, B. A. Buchine, B. Weintraub and Z. L. Wang, *Appl. Phys. Lett*., **91**, 142108 (2007**)**.
62. Y. Qin, R. Yang and Z. L. Wang, *J. Phys. Chem. C*, **112**, 18734 (2008); J. F. Jr. Conley, L. Stecker and Y. Ono, *Appl. Phys. Lett*., **87**, 223114 (2005).
63. S. Xu, Y. Ding, Y. Wei, H. Fang, Y. Shen, A. K. Sood, D. L. Polla and Z. L. Wang, *J. Am. Chem. Soc.*, **131**, 6670 (2009); S. Xu, Y. Shen, Y. Ding and Z. L. Wang, *Adv. Funct. Mater*., **20** 1493 (2010).
64. (a) S. H. Ko, I. Park, H. Pan, N. Misra, M. S. Rogers, C. P. Grigoropoulos and A. P. Pisano, *Appl. Phys. Lett.*, **92**, 154102 (2008). (b) V. Pachuri, A. Vlandas, K. Kern and K. Balasubramanian, *Small*, **6**, 589 (2010).
65. J. S. Lee, M. S. Islam and S. Kim, *Nano Lett.*, **6**, 1487 (2006).
66. S. Ju, J. Li, N. Pimparkar, M. A. Alam, R. P. H. Chang and D. B. Janes, *IEEE Trans. Nanotechnology*, **6**, 390 (2007).
67. Y. K. Park, H. S. Choi, J.-H. Kim, J.-H. Kim and Y.-B. Hahn, *Nanotechnolgy*, **22**, 185310 (2011).
68. H. J. Fan, B. Fuhrmann, R. Scholz, F. Syrowatka, A. Dadgar, A. Krost and M. Zacharias, *J. Cryst. Growth*, **287**, 34 (2006).
69. D. F. Liu, Y. J. Xiang, X. C. Wu, Z. X. Zhang, L. F. Liu, L. Song, X. W. Zhao, S. D. Luo, W. J. Ma, J. Shen, W. Y. Zhou, G. Wang, C. Y. Wang, S. S. Xie, *Nano Lett*., **10**, 2375 (2006).
70. Y. Masuda, N. Kinoshita, F. Sato and K. Koumoto, *Cryst. Growth & Design*, **6**, 75 (2006).
71. Y. Tak and K. Yong, *J. Phys. Chem. B*, **109**, 19263 (2005).
72. Q. Ahsanulhaq, J. H. Kim and Y. B. Hahn, *Nanotechnology*, **18**, 485307 (2007).
73. K.-P. Hsueh, S.-C. Huang, C.-T. Li, Y.-M. Hsin, J.-K. Sheu, W.-C. Lai, and C.-J. Tun, *Appl. Phys. Lett*., **90**, 132111 (2007); D. C. Oh, T. Suzuki, J. J. Kim, H. Makino, T. Hanada, M. W. Cho and T. Yao, *Appl. Phys. Lett*., **86**, 032909 (2005); S.-K. Hong, T. Hanada, H.-J. Ko, Y. Chen, T. Yao, D. Imai, K. Araki, M. Shinohara, L. Saitoh and M. Terauchi, *Phys. Rev. B*, **65**, 115331 (2002); T. Nakayama and M. J. Murayama, *J. Cryst. Growth*, **214-215**, 299 (2000); C.-W. Lin, D.-J. Ke, Y.-C. Chao, L. Chang, M.-H. Liang and Y.-T. Ho, *J. Cryst. Growth*, **298**, 472 (2007); Y. I. Alivov, U. Ozgur, S. Dogan, C. Liu, Y. Moon, X. Gu, V. Avrutin, Y. Fu and H. Morkoc, *Solid-State Electron*., **49**, 1693 (2005); H. J. Fan, F. Fleischer, W. Lee, K. Nielsch, R. Scholz, M. Zacharias, U. Gosele, A. Dadgar and A. Krost, *Superlattices Microstruct*., **36**, 95 (2004); W. I. Park and G. C. Yi, *Adv. Mater*., **16**, 87 (2004).
74. Q. Ahsanulhaq, A. Umar and Y. B. Hahn, *Nanotechnology*, **18**, 115603 (2007).
75. N. Koteeswara Reddy, Q. Ahsanulhaq and Y. B. Hahn, *Appl. Phys. Lett*., **93**, 083124 (2008).
76. N. Koteeswara Reddy, Q. Ahsanulhaq, J. H. Kim, M. Devika and Y. B. Hahn, *Nanotechnology*, **18**, 445710 (2007); N. Koteeswara Reddy, Q. Ahsanulhaq, J. H. Kim and Y. B. Hahn, *Appl. Phys. Lett*., **92**, 043127 (2008).
77. K. Keis, C. Bauer, G. Boschloo, A. Hagfeldt, K. Westermark, H. Rensmob and H. Siegbahn, *J. Photochem. Photobio. A: Chem.*, **148**, 57 (2002).
78. K. Kakiuchi, E. Hosono and S. Fujihara, *J. Photochem. Photobio. A: Chem.*, **179**, 81 (2006).
79. J. B. Baxtera and E. S. Aydil, *Appl. Phys. Lett.*, **86**, 053114 (2005); J. B. Baxtera and E. S. Aydil, *Sol. Ener. Mater. Sol. Cells*, **90**, 607 (2006).
80. M. Law, L. E. Greene, J. C. Johnson, R. Saykally and P. Yang, *Nature Mater*., **4**, 455 (2005); L. E. Greene, B. D. Yuhas, M. Law, D. Zitoun and P. Yang, *Inorg. Chem*., **45**, 7535 (2006).
81. S. H. Ko, D. Lee, H. W. Kang, K. H. Nam, J. Y. Yeo, S. J. Hong, C. P. Grigoropoulos and H. J. Sung, *Nano Lett*., **11**, 666 (2011).
82. Z. L. Wang and J. H. Song, *Science*, **312**, 242 (2006).
83. M.-P. Lu, J. Song, M.-Y. Lu, M.-T. Chen, Y. Gao, L.-J. Chen and Z. L. Wang, *Nano Lett*., **9**, 1223 (2009).
84. G. Zhu, R. Yang. S. Wang and Z. L. Wang, *Nano Lett*., **10**, 3151 (2010).
85. A. Umar, M. M. Rahman, S. H. Kim and Y. B. Hahn, *J. Nanosci*.

Nanotechnology, **8**, 3216 (2008).
86. A. Umar, M. M. Rahman, M. Vaseem and Y.-B. Hahn, *Electrochem. Commun.*, **11**, 118 (2009).
87. A. Umar, M. M. Rahman, A. Al-Hajry and Y.-B. Hahn, *Talanta*, **78**, 284 (2009).

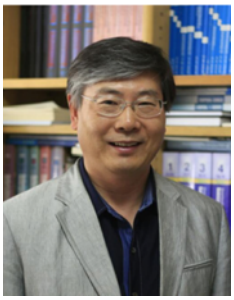

Dr. Yoon-Bong Hahn is Director of BK21 Center for Future Energy Materials and Devices, Head of School of Semiconductors and Chemical Engineering, and WCU Professor in Dept. of BIN Fusion Technology at Chonbuk National University (CBNU), Korea. He joined CBNU in 1991, prior to which he worked for LG Metals Research Center for 1988-1991 after he received his Ph.D in Dept. of Metallurgical Engineering, University of Utah in 1988. His research has resulted in over 190 peer-reviewed SCI papers and over 300 presentations at domestic and international conferences. He co-edited 4 books including Metal Oxide Nanostructures and Their Applications (5 volume sets) published by American Scientific Publishers (ASP) in March 2010. He is also the inventor of several patents, including key patents on the hybrid green energy window system, the thin film transistors having various structures containing laterally grown nanowires, and piezoelectric nanomaterials based biomimetic devices. He received The Scientist of Month Award in July, 2011, conferred by Korea Ministry of Education, Science and Technology. In 2005 and 2011 he was also honoured as Top 100 Scientists accredited by International Biographical Center, Cambridge, UK. He received several best paper awards in renowned international conferences and won Best Research Professor Award at CBNU for three consecutive years (2007-2009). His research area is growth of metal and metal oxide nanostructures and their applications for solar cells, optoelectronics, and biosensors and biomimtic devices.